

AperTO - Archivio Istituzionale Open Access dell'Università di Torino

The duality of UiO-67-Pt MOFs: connecting treatment conditions and encapsulated Pt species by operando XAS

This is the author's manuscript

Original Citation:

Availability:

This version is available <http://hdl.handle.net/2318/1651672> since 2018-04-03T16:57:00Z

Published version:

DOI:10.1039/c7cp05185a

Terms of use:

Open Access

Anyone can freely access the full text of works made available as "Open Access". Works made available under a Creative Commons license can be used according to the terms and conditions of said license. Use of all other works requires consent of the right holder (author or publisher) if not exempted from copyright protection by the applicable law.

(Article begins on next page)



UNIVERSITÀ DEGLI STUDI DI TORINO

This is an author version of the contribution published on:

Questa è la versione dell'autore dell'opera:

Physical Chemistry Chemical Physics, 19, 40, 2017, DOI: 10.1039/c7cp05185a

The definitive version is available at:

La versione definitiva è disponibile alla URL:

<http://pubs.rsc.org/en/Content/ArticleLanding/2017/CP/C7CP05185A#!divAbstract>

The duality of UiO-67-Pt MOFs: connecting treatment conditions and encapsulated Pt species by *operando* XAS

L. Braglia,^{a,b,*} E. Borfecchia,^a A. Martini,^a A. L. Bugaev,^{a,b} A. V. Soldatov,^b S. Øien-Ødegaard,^c B. T. Lønstad-Bleken,^c U. Olsbye,^c K. P. Lillerud,^c K. A. Lomachenko,^{b,d} G. Agostini,^{d,e} M. Manzoli^f and C. Lamberti^{b,g,*}

^a Department of Chemistry, NIS Interdepartmental Centre and INSRM reference centre, University of Turin, via Quareello 15A, I-10135 Turin, Italy.

^b IRC “Smart Materials”, Southern Federal University, Zorge Street 5, 344090 Rostov-on-Don, Russia.

^c inGAP Centre for Research Based Innovation, Department of Chemistry, University of Oslo, Oslo, Norway.

^d European Synchrotron Radiation Facility (ESRF), 71 Avenue des Martyrs, CS 40220, 38043 Grenoble Cedex 9, France.

^e Leibniz Institute for Catalysis at the University of Rostock (LIKAT), Albert-Einstein-Str. 29A, D-18059 Rostock, Germany.

^f Department of Drug Science and Technology, NIS Interdepartmental Centre, University of Torino, Via P. Giuria 9, 10125 Torino, Italy.

^g Department of Chemistry, CrisDi Interdepartmental Centre and INSRM reference University of Turin, via Pietro Giuria 7, 10125 Turin, Italy

* Corresponding authors, e-mails: luca.braglia@unito.it; carlo.lamberti@unito.it

Abstract We report an X-ray absorption spectroscopy (XAS) study of the UiO-67 Pt-functionalized metal organic frameworks (MOFs), demonstrating that, in proper conditions, at least two types of catalytically active sites can be formed in the cavities of the MOF, including isolated Pt-complexes and Pt nanoparticles (Pt-NPs). Both pre-made linker synthesis (PMLS) and post-synthesis functionalization (PSF) methods were adopted. The classic UiO-67 linker is the biphenyl-dicarboxylate (bpdc) while for grafting a transition metal to the MOF bipyridine (bpydc) linkers are employed. In PMLS, both H₂bpdc and PtCl₂-(H₂bpydc) are included in the MOF synthesis to yield a mixed linker MOF as product. Conversely, PSF method consists in the synthesis of UiO-67-bpdc already with a percentage of substituted bpydc linkers that, afterwards, can react with K₂PtCl₄. XAS was used to monitor the temperature-dependent behaviour of UiO-67-Pt while heating from RT to 623 K, in different gas feeds (pure He, 3% H₂/He and 10% H₂/He). We collected static *in situ* Pt L_{III} XANES and EXAFS spectra at RT before and after the thermal treatment, as well as spectra acquired under *operando* conditions upon heating. The *in situ* EXAFS analysis, for all the series of samples at RT, demonstrates that the Pt atoms are grafted to the bpydc-linkers in square planar coordination with two Cl and two N atomic neighbours. In 10% H₂/He, the Fourier-transform EXAFS spectra clearly show the loss of Cl and N scattering contributions, while the rising of an intense signal associated to the Pt-Pt contributions, unambiguously indicates Pt-NPs formation. The Pt-NPs formation has been followed with a parametric EXAFS analysis of the data collected during temperature programmed H₂-reduction (TPR), using the Einstein model to predict the temperature dependence of the Debye-Waller factors. Conversely, in pure He flow, the only significant change observed during TPR is the progressive decrease of the Pt-Cl single scattering contribution, leading to the conclusion that the Pt grafted to the bpydc-linkers remains naked. Advanced EXAFS/TEM analysis allowed us to quantify the fraction of the Pt in form of Pt NPs, values that have been quantitatively confirmed by linear combination analysis of the XANES spectra. *Operando* XANES experiments were supported by quasi simultaneous X-ray powder diffraction (XRPD) data collection testifying the resistance of the UiO-67 framework to TPR. *In situ* XANES/EXAFS study were supported by *ex-situ* XRPD and BET analyses, confirming the framework stability and testifying a loss of the internal volume after TPR due to the formation of Pt NPs insides the MOF pores, more relevant in the sample where smaller Pt NPs were formed.

1. INTRODUCTION

In the last decades, the discovery of new types of metal organic framework (MOFs) raised exponentially.¹⁻¹⁷ In particular, in the present work, we focused our attention on their employment as support for active metal sites in heterogeneous catalysis.¹⁸⁻²² However, metal sites in most of the MOF structures show at maximum one coordination vacancy (and only after removal of the solvent, see e.g. the HKUST-1^{23, 24} and the CPO-27²⁵⁻²⁷), therefore limiting their application in catalysis, where at least two coordination vacancies are required. In this regard, the functionalization of MOF materials is one of the main challenges driving the MOF community,²⁸⁻⁴¹ to make newer and newer structures, with specific functionalities.

Among the many classes of MOFs, the UiO-66/67/68 family⁴²⁻⁵² shows an incredible thermal and chemical stability. The UiO-66/67/68 frameworks are obtained by connecting the 12-fold coordinated $Zr_6O_4(OH)_4$ inorganic cuboctahedron with organic linkers of increasing length 1,4-benzene-dicarboxylate, (bdc), 4,4'-biphenyl-dicarboxylate (bpdc) or 4,4'-terphenyl-dicarboxylate (tpdc) respectively.⁴² Because of the high stability, this class of materials is an attractive candidate for a variety of applications in the fields of catalysis,⁵³⁻⁶¹ H_2 ,⁴⁴ CH_4 ,^{62, 63} and CO_2 ^{61, 64, 65} uptake, proton conduction,^{66, 67} removal of air⁶⁸ and water⁶⁹ contaminants, gas separation,⁷⁰⁻⁷² sensor applications,⁷³ and for radioactive waste scavenging.⁷⁴

Also in the case of UiO-66/67/68, functionalization has played an important role in enhancing the material potentialities. Among all, we mention: functionalization by insertion of other metals in the inorganic cornerstone $M_xZr_{6-x}O_4(OH)_4$ ($M = Hf, Ce, Ti$);⁷⁴⁻⁷⁶ functionalization by controlled defect engineering (missing linkers, metal centers or inorganic cornerstones);^{46, 49, 50, 53, 54, 64, 77-80} bromo, nitro, and naphthalene functionalization of UiO-66/67;^{21, 81-83} proline functionalization of UiO-67/68⁸⁴; functionalization by use of biphenyl-, terphenyl-, and quaterphenyl-based linkers;⁸⁵ N-quaternization of the pyridine sites of UiO-67.⁶⁵

With this respect, there are multiple choices of relatively easy ways to functionalize the linker of the UiO-67 with metal sites by substituting a fraction of the standard bpdc linkers with bipyridine-dicarboxylate (bpydc) linker, as described in the experimental section. In such a way, Fe(II),⁸⁶ Ni(II),⁸⁷ Cu(II),⁸⁸⁻⁹² Ru(II),⁹³ Rh(III),^{94, 95} Pd,⁹⁶ Re(I),⁹³ Ir(III),^{93, 95} Pt(II),^{92, 97-99} and Pt(IV),^{92, 98, 99} have already been successfully grafted to the two N atoms of the functionalized bpydc linker of different MOFs. In this paper, we present a study done on UiO-67 functionalized with Pt, metal chosen for its extensive and interesting chemistry in catalysis. Indeed, Pt-based catalysts are used in a wide range of industrial applications, which include proton exchange in membrane fuel cells,¹⁰⁰ industrial synthesis of nitric acid,¹⁰¹ oxidation of CO and NO_x in the exhaust gases from vehicles (Pt is one of the components of the catalytic converter),^{102, 103} hydrogenation of nitro compounds to amines¹⁰⁴ and from ketones to alcohols.¹⁰⁵ In many of these reactions, a central role is covered by zero-valent Pt nanoparticles, usually supported on high surface area oxides, zeolites or carbons. In general, the catalytic activity per metal atom increases while decreasing the size of metal particles, therefore development of an experimental procedure to lower the metal particles to nano-, subnano- and even single-atom size is a very attractive topic.¹⁰⁶ Due to their extraordinarily high surface area and well-defined pore structure, MOFs can be used for the stabilization of metal

nanoparticles with adaptable size and narrow size distribution.^{107, 108} The important fact is that the embedded metal nanoparticles are still accessible for other reagents due to the high porosity of the MOF systems. Moreover, Na *et al.*¹⁰⁹ have shown how Pt NPs deposited on the UiO-66 and UiO-67 or embedded in their cavities achieved different products and selectivity during the reaction with methylcyclopentane. In this study, we found out that tuning the H₂ flow during the thermal treatment of the UiO-67-Pt allows tuning the nature of encapsulated Pt-species, from isolated framework Pt(II) exhibiting two coordination vacancies (potentially interesting for C–H bond activation)¹¹⁰⁻¹¹⁵ to very small Pt NPs hosted inside the MOF cavities, potentially interesting for hydrogenation reactions.¹¹⁶ In addition, we compared during the same treatment the behavior of UiO-67 functionalized with different Pt contents and two synthesis methods. The former involves premade linker synthesis (PMLS) in which PtCl₂(H₂bpydc) is used as organic secondary building units in the MOF synthesis, and the latter concerns in a post synthesis functionalization (PSF) where a platinum chloride solution is reacted with UiO-67 with open bpydc sites.⁹⁸ We performed XAS spectroscopy for all the samples *in situ* and *operando* conditions; by means of X-ray absorption spectroscopy near-edge structure (XANES) we monitored the oxidation state of Pt, while analyzing extended X-ray absorption fine structure (EXAFS) we observed the loss of Cl ligands during the thermal treatment and the formation of Pt NPs, also confirmed by TEM measurements. *Operando* XANES experiments were supported by quasi simultaneous X-ray powder diffraction (XRPD) data collection testifying the resistance of the UiO-67 framework to the temperature programmed H₂-reduction (TPR). In situ XANES/EXAFS study were supported by ex-situ XRPD and BET analyses. The former confirmed the framework stability while the latter testified a loss of the internal volume due to the formation of Pt NPs inside the MOF pores.

In summary, herein we verify that Pt functionalized UiO-67 can lead to either bpydc-Pt(0) linker, already studied by Øien *et al.*,⁹⁸ or to Pt-NPs, discussed in more details in this work, and that the relative ratio between the two species can be tuned by controlling activation conditions. Moreover, we compare the Pt-NPs formation in Pt functionalized UiO-67 synthesized in different ways (PMLS or PSF) and with different Pt content (2.8% wt. and 5.5% wt.).

2. EXPERIMENTAL AND METHODS

2.1 Materials synthesis.

We investigated a series of UiO-67 MOFs functionalized with Pt precursors. Pre-made linker synthesis (PMLS) and post-synthesis functionalization (PSF) were adopted for incorporating the Pt in the MOFs.⁹⁸ The classic UiO-67 linker is the biphenyl-dicarboxylate (bpdc),⁴⁴ while for grafting a transition metal to the MOF, Pt in this work, bipyridine (bpydc) linkers are employed.⁹⁸ A detailed description of the synthesis and functionalization procedures follows.

DMF and demineralized H₂O were added to a 250 mL Erlenmeyer flask with a magnetic stirring bar. ZrCl₄ was slowly added to the solution, and completely dissolved. The slow addition was found to be particularly important, as it reacts exothermically with water. Then, the benzoic acid was added and dissolved rapidly. The flask was then heated up to 110 °C while

stirring. bpdc and bpydc linkers (or (PtCl₂)bpydc in the case of PMLS) were added simultaneously and gradually over a short period (~30 seconds). A clear solution was obtained shortly after the addition. Afterwards, the stirring bar was removed and the flask was placed in an oven at 120 °C for two days. The solvent was removed using vacuum filtration and the residual, white (or yellow) slurry was added back into the flask. About 50 mL of DMF was added to the flask together with a stirring bar. The mixture was then stirred overnight to remove residual modulator at 40 °C. The solvent was then removed by using a vacuum filtration setup. 50 mL of THF was then added, and the mixture was stirred for two to three hours. THF was removed using a vacuum filtration setup and an extra 30 mL of THF was used to wash the powder on the filter. After filtrating, the powder was collected in an uncovered glass vial and put in an oven at 60 °C overnight to remove THF. The next day the temperature was increased to 200 °C to remove any residual high boiling point species, and the white (or yellow in case of PMLS) powder was recovered after drying overnight.

For the PSF method, 1 g of the parent UiO-67-bpy (5-10%) was mixed with 150 mL DMF in a 250 mL round bottom flask. The mixture was then sonicated for one hour to disperse the UiO-67-bpy powder. Afterwards, the round bottom flask was transferred to a hotplate with an oil bath. While stirring, K₂PtCl₄ (in a 25 % molar excess in respect to the expected number of bpy sites) was slowly added. A reflux condenser was then connected to the flask and the mixture was heated up to 100 °C overnight. Within the first few hours the red crystals were observed to dissolve to give a red slurry. The next day, the MOF slurry had turned yellow, which indicated the coordination of platinum to the bpydc linker. The powder was collected using a vacuum filtration setup. Any remaining powder inside the flask was mixed with 30 mL DMF and added to the filtration. The yellow slurry residual was transferred back into the round bottom flask and 50 mL DMF was added. The mixture was then stirred for one hour under heating at 100 °C using the oil bath and reflux condenser again. The purpose of this washing step was to remove any excess K₂PtCl₄ that is not coordinated to the bpydc linker. Afterwards, the powder was collected again through a vacuum filtration setup. This washing step with hot DMF was repeated once. 50 mL of THF was then added, and the mixture was stirred for 15 minutes. THF was removed using a vacuum filtration setup and an extra 30 mL of THF was used to wash the powder on the filter. This step was repeated twice. After filtrating, the powder was collected in an uncovered glass vial and put in an oven at 60 °C overnight to remove THF. The temperature was increased to 150 °C and the yellow powder was recovered after drying overnight.

Table 1. Abbreviation names, and quantitative synthesis details for the samples.

Chemical	5PMLS		10PMLS		10PSF	
	Molar ratio	Mass (g)	Molar ratio	Mass (g)	Molar ratio	Mass (g)
DMF	300	94.4	300	94.4	300	94.4
ZrCl ₄	1	1.003	1	1.003	1	1.003
H ₂ O	3	0.23	3	0.23	3	0.23
Benzoic acid	10	5.258	10	5.258	10	5.258
bpdc	0.95	0.991	0.9	0.939	0.9	0.939
(PtCl ₂)bpdc	0.05	0.11	0.1	0.22	–	–
bpydc	–	–	–	–	0.1	0.105

K ₂ PtCl ₄	–	–	–	–	0.125	0.022
Yield (g)		1.15		1.13		1.18
Yield (%)		73%		69%		72%
Pt wt%		2.8		5.5		5.5

In particular, the samples investigated in this work are: UiO-67-5%*H₂bpydc*-PtCl₂ (PMLS) with 2.8% wt. of Pt, UiO-67-10%*H₂bpydc*-PtCl₂ (PMLS) with 5.5% wt. of Pt and UiO-67-10%*H₂bpydc*-PtCl₂ (PSF) with 5.5% wt. of Pt (where 5% and 10% indicates the employed percentage of *bpydc*-linkers). For the sake of brevity, in the following we will use the abbreviated names listed in Table 1 for the samples labelling: (5PMLS, 10PMLS and 10PSF).

2.2. Laboratory characterization set-ups: N₂ adsorption isotherms, XRPD and TEM.

PXRD patterns were acquired using a Bruker D8 Discover diffractometer with Cu K_{α1}-radiation in reflection geometry. Nitrogen sorption measurements were performed on a BelSorp mini II instrument at 77 K. All samples were measured in 9.001 cm³ glass cells. Prior to adsorption measurements the samples were pretreated (activated) under vacuum for 1 h at 80°C and 2 h at 200°C. Brunauer-Emmett-Teller (BET) surface areas¹¹⁷ were calculated by fitting the isotherm data in the *p/p₀* range 0 - 0.1, meeting the established consistency criteria.¹¹⁸

Transmission electron microscopy (TEM) and high resolution TEM (HR-TEM) measurements were performed by using a Jeol 3010-UHR electron microscope operating at 300 kV, equipped with a LaB₆ filament and with an Oxford Inca Energy TEM 300 EDS X-rays analyzer by Oxford Link. Digital micrographs were acquired by means of a (2k × 2k)-pixel Gatan Ultrascan 1000 CCD camera and processed by Gatan digital micrograph. Before the experiments, the reduced powders were milled in an agate mortar and deposited on a copper grid covered with a lacey carbon film. A statistical evaluation of the size of the Pd particles was carried out for each material. Histograms of the particle size distribution were obtained by considering at least >1250 nanoparticles on the collected images, and the mean particle diameter (*d_m*) was calculated as $d_m = \sum d_i n_i / \sum n_i$, where *n_i* was the number of particles of diameter *d_i*. The counting was carried out on electron micrographs acquired starting from 100000× magnification, where roundish Pt nanoparticles contrasted with respect to the support were detected.

2.3. Operando XANES using a capillary reactor.

We performed *operando* XANES experiments at the BM01B beamline of the European Synchrotron Radiation Facility (ESRF, Grenoble, France, now moved to port BM31)^{119, 120} aiming to monitor the dual behavior of UiO-67 Pt functionalized MOFs upon the thermal treatment from room temperature (RT) to 623 K and in different gas feeds (0, 3 and 10 % *H₂*/*He*) and to simultaneously check the structural stability of UiO-67-Pt framework by XRPD. The beamline allows a rapid (about 30 s) plug and play switch between X-ray absorption and

X-ray diffraction setups, allowing to both EXAFS and XRPD on exactly the same sample conditions.¹²¹

The operation energy at the ESRF was 6 GeV with ring current ranging from 200 to 160 mA (and a lifetime of about 50 h). The white beam, coming from the bending magnet, was monochromatized by water-cooled double crystal Si(111) monochromator and shaped by a horizontal slit according to the length of catalytic bed and detuned to avoid the third harmonic contribution.¹²² We worked in transmission mode at Pt L_{III}-edge (11564 eV). We employed 30 cm-ionizations chambers to measure the incident, I_0 , and transmitted, I_1 , intensities, with N₂ and Ar gases to guarantee 12% and 75% of absorption, respectively. The intensity I_2 transmitted by a Pt reference foil located after the second ionization chamber was measured simultaneously using a third ionization chamber, and the resulting spectra were employed for energy alignment.¹²³

X-ray powder diffraction was measured using $\lambda = 0.51353(1)$ Å radiation, selected by a Si(111) channel-cut monochromator. CMOS-Dexela 2D detector which covered the 2θ range up to 32° ($d_{\min} = 0.93$ Å), the values below 4° were not used in the refinement because the scattered intensity was affected by the beam-stop. The λ value, the sample to detector distance and detectors tilts have been optimized by Rietveld refinement of NIST LaB₆ and Si samples and kept fixed in the refinement of the UiO-67 patterns. For better statistics 20 diffraction images and 20 dark images (without X-ray beam) with acquisition time of 1 second were collected at each of the external conditions. 2D XRPD patterns were processed by PyFAI¹²⁴ software which executes fast averaging, background subtraction and integrating of images to obtain $I(2\theta)$ patterns. Rietveld refinement was performed in Jana2006 code.¹²⁵

The as-prepared powdered MOF samples were packed into 1.5 mm quartz glass capillaries with quartz wool supporting both sides of the bed and additional tubing was accommodated to control the gas stream. The capillary diameter was optimized for XRPD, resulting in an edge jump at the Pt L_{III}-edge of $\Delta\mu_x = 0.08$ only, still allowing good quality XANES spectra to be obtained. The catalytic bed was packed to be about 5 mm long, which resulted in sample mass of ca. 3 mg. An electronic flow meter was used to adjust the flow through the bed in order to have typically 1 ml/min for each 2 mg of catalyst. Gas controlled system (mass flow controller, valves) was driven and monitored in remote from the control room.

2.4. *In situ static XANES and EXAFS experiments before and after TPR using a cell for pelletized samples.*

Based on the results obtained in the experiments at the BM01B beamline, we repeated the temperature-programmed reduction (TPR) in the RT-623 K range in 10% H₂ for the all series of samples, using a different *ad hoc* cell designed for high-quality EXAFS data collection on pelletized samples using a home-designed reaction cell,¹²⁶ see Figure S8 of the ESI for a photographic description of the set-up.

We collected the data at I811 beamline in Max Lab II (Lund, Sweden),^{127, 128} operating at 1.5 GeV with a current ranging from 250 and 100 mA. A liquid He-cooled superconducting wiggler was employed to produce the white beam, subsequently monochromatized by a

horizontally sagittally focused double-crystal Si(111) monochromator, detuned to 20% to minimize the third harmonic at around 35 keV.¹²² We performed the experiment in transmission mode at the Pt L_{III}-edge; the I₀ and I₁ were measured by 30 cm-ionization chambers using a mixture of Ar and N₂ gases to guarantee an absorption of 12% and 75%, respectively. We acquired three spectra for each static condition of the sample: in He at RT, at 623 K in H₂ at the steady state, and at RT after the TPR. For the static measurements, the spectra were collected in quick-EXAFS mode¹²⁹ covering the energy range from –200 eV to 1680 eV from the absorption edge in 600 s at constant angular speed. The extraction of the $\chi(k)$ was performed with the Athena code.¹³⁰ The Artemis code¹³⁰ was used to analyze the EXAFS spectra at RT before and after the TPR. The averaged $k^2\chi(k)$ function were Fourier Transformed (FT) in $\Delta k = 3.1\text{--}17.0 \text{ \AA}^{-1}$ interval. The fits were performed on the averaged spectra¹³¹ in R-space in $\Delta R = 1.0\text{--}4.8 \text{ \AA}$ range ($2\Delta k\Delta R/\pi > 33$). The employed scattering paths were calculated with FEFF6 code¹³² using the [bpydc-PtCl₂] DFT-optimized structure of the MOF-linker, previously reported by Borfecchia *et al.*⁹⁹ Overall, the analysis confirmed the EXAFS results reported in our previous work.⁹⁸ After the thermal treatment, apart from the [bpydc-PtCl₂] input structure, we introduced in the EXAFS fit also the paths related with the Pt metal component, fundamental for fitting the contributions associated to the Pt nanoparticles (Pt-NPs).

2.5. Operando TPR-EXAFS experiments using a cell for pelletized samples.

Operando temperature programmed H₂-reduction (TPR) was done fluxing 10% H₂ in He with a flow of 100 ml min^{–1} inside the cell and increasing the temperature by 5 K min^{–1} until 623 K. Each quick-EXAFS spectrum ranges from –200 to 1210 eV from the edge with a total acquisition time of 360 s, giving a temperature-resolution of the experiment of $\Delta T = 30 \text{ K}$. We acquired a series of EXAFS spectra from RT to 623 K and waiting at 623 K until there were no further changes in the XAS features. Athena code¹³⁰ was also used for the extraction of the $\chi(k)^2$ functions of the spectra collected during the TPR experiments. Parametric EXAFS data analysis on the whole series of spectra was performed using the IFEFFIT code.¹³³ Extracted $k^2\chi(k)$ function were Fourier transformed in the $\Delta k = 3.2\text{--}13.4 \text{ \AA}^{-1}$ interval. The fits were performed in R-space in the $\Delta R = 1.0\text{--}3.1 \text{ \AA}$ range (number independent points: $2\Delta k\Delta R/\pi > 13$). As the heating ramp of the TPR was 5 K min^{–1}, EXAFS spectra were recorded with a temperature resolution of 30 K. We used the same phase and amplitude functions employed to model the Pt–N, Pt–Cl (for bpydc-PtCl₂ linker)^{98–99} and the Pt–Pt (for Pt metal foil) single scattering (SS) paths in the analysis of the static EXAFS spectra. The main purpose of the TPR-EXAFS experiment was to monitor when and how the Pt-NPs were formed. The analysis of *operando* EXAFS during TPR is entangled by the presence of three SS paths related with at least two different Pt-species (framework bpydc-PtCl₂ and Pt-NPs) but mostly by the strong correlation between coordination numbers (N_N , N_{Cl} and N_{Pt}) and the corresponding Debye-Waller (DW) factors of N, Cl and Pt atoms (σ_N^2 , σ_{Cl}^2 and σ_{Pt}^2). DW factors, by definition, depend on the temperature,¹³⁴ thus in a temperature-dependent experiment they are not constant. Hence, we adopted the Einstein model¹³⁵ to predict this dependence in the temperature-dependent EXAFS spectra.^{98, 136–144} The details of the strategy for TPR-EXAFS analysis is described *item by item* in the following, distinguishing four subsequent refinement steps.

2.5.1. First Refinement Step. In this first step, considered as a preliminary consistency test, each EXAFS spectrum of the temperature-dependent series has been analyzed independently from the others. We refined the σ^2_{N} , σ^2_{Cl} and σ^2_{Pt} parameters and one independent ΔE common to both Pt–N and Pt–Cl paths (being the energy shift of the Pt–Pt paths, ΔE_{metal} , constrained to $\Delta E_{\text{metal}} = \Delta E - 2.7$ eV, from the refinement of the $\text{PtCl}_2(\text{H}_2\text{bpydc})$ linker, see Table 3). Conversely, the S_0^2 of the two phases and the three bond distances ($R_{\text{Pt–N}}$, $R_{\text{Pt–Cl}}$ and $R_{\text{Pt–Pt}}$) have been fixed to the values obtained in the refinement of the EXAFS spectrum collected in static conditions at RT in a higher k-range. The N_{N} , N_{Cl} and N_{Pt} were refined for all data sets. Within the experimental incertitude, a constant value around 2 was observed for both N_{N} and N_{Cl} along the whole heating step till 623 K; for all these data N_{Pt} resulted in a non-physical trend jumping from positive to negative values (compatible with zero in the error). In the isotherm at 623 K a significant decay of both N_{N} and N_{Cl} is observed, accompanied by a parallel increase of N_{Pt} , following a meaningful trend. As it can be appreciated in Figure S1 of the ESI, all refined parameters are subjected to large relative errors caused by a significant number of variables that correlate.

2.5.2. Second Refinement Step. To better appreciate temperature where the model adopted is not any more able to reproduce experimental data Pt–Pt SS (not needed in the first part of the temperature ramp) was excluded and coordination numbers (N_{N} and N_{Cl}) were both imposed equal to two to avoid the correlation with the σ^2_{N} and σ^2_{Cl} parameters. Therefore, we constrained our fitting model to only account for the presence of stable bpydc-PtCl_2 linkers, during the whole thermal treatment. Afterwards, by plotting σ^2_{N} and σ^2_{Cl} as a function of time during TPR, see Figure S1, we identified the temperature (T_1) when the DW factors begin to be unphysical and instable. In the temperature interval between RT and T_1 , both σ^2_{N} and σ^2_{Cl} values increase linearly with T , as expected from the Debye or Einstein models,^{138, 143, 145-147} for temperature considerably lower than that needed to break the bond. This linear behaviour guarantees that all Pt sites are in the form of undamaged bpydc-PtCl_2 linkers.

2.5.3. Third Refinement Step. Considering the subset of spectra belonging to the linear region mentioned above, we have then performed a parametric refinement, commonly adopted in XRPD Rietveld refinements,^{148, 149} of the TPR-EXAFS spectra implementing the Einstein model for describing the temperature dependence of the σ^2_{N} and σ^2_{Cl} factors. The assumption in the Einstein model is that all atoms oscillate independently at the same single frequency called Einstein frequency (ω_E). The model assumes that both Pt–N (or Pt–Cl) bonds behaves as a quantum harmonic oscillator of mass equal to the reduced mass of the atomic pair ($M = 13.070$ and 30.004 amu for the Pt–N and Pt–Cl pairs, respectively). The behaviour of $\sigma^2(T)$ is determined only by the ω_E parameter, according to the equation:

$$\sigma^2(T) = \frac{\hbar}{2M\omega_E} \coth \left[\frac{\hbar\omega_E}{2k_B T} \right] = \frac{\hbar^2}{2Mk_B\Theta_E} \coth \left[\frac{\Theta_E}{2T} \right] \quad (1)$$

The Einstein temperature Θ_E of the Pt–N (or Pt–Cl) bond is related to the Einstein frequency by the relationship: $\hbar\omega_E = k_B\Theta_E$, where $\hbar = 1.055 \times 10^{-34}$ J s is the reduced Plank constant and $k_B = 1.38 \times 10^{-23}$ J K⁻¹ is the Boltzmann constant. The N_N and N_{Cl} were set to 2 because in the linear region we assumed only the presence of the bpydc-PtCl₂ linker, already verified in the first and second refinement steps. In this way, we obtained the Einstein temperature for the Pt–N and Pt–Cl that are reported in Table 2.

Table 2. Summary of the Einstein Temperatures Θ_E obtained for both Pt–N and Pt–Cl bonds in the TPR-EXAFS experiments

Sample	$\Theta_E(\text{Pt–N})$ (K)	$\Theta_E(\text{Pt–Cl})$ (K)
5PMLS	865±57	511±13
10PMLS	783±46	458±10
10PSF	691±35	383±8

2.5.4. Fourth, and Final, Refinement Step. In the fourth refinement, the Pt–Pt SS path was considered again, optimizing the N_{Pt} and the σ^2_{Pt} . As already done in the first refinement, ΔE_{metal} was constrained to the ΔE of the Pt(II) species in bpydc-PtCl₂, according to the equation: $\Delta E_{\text{metal}} = \Delta E - 2.7$ eV. Then the whole series of EXAFS spectra were analyzed optimizing the coordination numbers (N_N , N_{Cl}), being the two Debye–Waller factors (σ^2_N and σ^2_{Cl}) fixed to the value obtained from eq. (1) and from the Θ_E parameters determined in the third refinement step, see Table 2.

3. RESULTS AND DISCUSSION

3.1 Determination of the Pt local environment in as-prepared UiO-67-Pt by static EXAFS.

According to our previous study,⁹⁸ the EXAFS spectra of the three as-prepared samples were analysed using the [PtCl₂(H₂bpydc)] optimized model, whose structure is reported in the inset of Figure 1a. This structure consists of the Pt atom in square-planar coordination with two N atoms of the bpydc-linker and two Cl atoms. Parts (a) and (b) of Figure 1 report the moduli and imaginary parts of the k^2 -weighted, phase uncorrected, FT of the experimental EXAFS spectra of 5PMLS, 10PMLS and 10PSF samples. For comparison, Figure 1 reports also the corresponding spectra for the PtCl₂(H₂bpydc) linker (grey curve). All moduli of FTs are characterized by two defined peaks at 1.67 Å and at 1.94 Å due to the first shell SS contributions from N and Cl atoms, respectively, followed by a complex structure in the 2.3–4.0 Å due to a large number of SS and MS paths involving N and C atoms of the linker.

The position and the intensity of the EXAFS features for the samples synthesized by PMLS method are the same as that of the linker, while the 10PSF presents a slightly lower intensity for the two peaks at 1.67 Å and at 1.94 Å, as better appreciated Figure S2b,c, where the curves of the different samples are reported without a vertical shift. The position of the signals of N and Cl in the modulus of FT (see Figure 1a and S2b) are partially overlapped, thus it is difficult

to distinguish which atomic species is responsible of the decrease of intensity. Instead, in the imaginary part of FT (see Figure 1b and S2c) the differences between the two atomic contributions can be resolved more easily, highlighting an average lack of Cl ligands in PSF MOFs with respect to PMLS samples and with respect to the $\text{PtCl}_2(\text{H}_2\text{bpydc})$ linker (grey curve). In general, the lower signal in the FT could be interpreted also with a higher degree of inhomogeneity in the PSF sample. However, this alternative hypothesis can be ruled out looking to the data in k-space (Figure S2a) where no particular dumping is observed in the high k-region for the spectrum of the 10PSF sample. This observation, joined with the fact that the high R-region of the FT of sample 10PSF corresponds to that of the $\text{PtCl}_2(\text{H}_2\text{bpydc})$ linker, allows us to conclude a full grafting of the Pt(II) species to the framework sites, with a lower coordination number of Cl in 10PSF. These qualitative insights were confirmed by EXAFS fits on the whole sample series. The fits were performed by guessing a passive amplitude reduction factor S_0^2 common for all three MOF samples, for a more robust identification of slight differences in the average Pt coordination environment as a function of preparation protocol/Pt-loading. The optimized value ($S_0^2 = 0.94 \pm 0.04$) well agrees with the corresponding value optimized for the $\text{PtCl}_2(\text{H}_2\text{bpydc})$ linker ($S_0^2 = 0.93 \pm 0.05$), see Table 3. The numerous SS and multiple scattering (MS) paths of the C atoms in the bpydc-linker were considered using a “collective” parametrization strategy for the whole bpydc unit.^{24, 25, 91, 150-152} In particular, these paths were modelled using an isotropic global contraction/expansion factor α_{bpydc} and a DW factor σ_{bpy}^2 increasing as the square root of the effective distance $R_{\text{eff},i}$ ($\Delta R_{\text{bpy},i} = \alpha_{\text{bpydc}} R_{\text{eff},i}$, $\sigma_{\text{bpydc},i}^2 = \sigma_{\text{bpydc}}^2 (R_{\text{eff},i}/R_N)^{1/2}$, where $R_{\text{eff},i}$ corresponds to the interatomic distances for the SS contributions and to half of the overall scattering path for the MS ones and $R_N = 2.00 \text{ \AA}$). This approach allows to optimize only two parameters: α_{bpydc} , σ_{bpydc}^2 , with obvious benefit in keeping correlations among optimized parameters as low as possible.^{24, 25, 91, 152} All the parameters were guessed and we obtained meaningful results with S_0^2 close to unit (0.94), and correlations among parameters below 0.8 in modulus. For both 5PMLS and 10PMLS samples, the coordination numbers of all paths have been fixed to the stoichiometric values of the model in the inset of Figure 1a. All obtained values are fully comparable with those obtained on the $\text{PtCl}_2(\text{H}_2\text{bpydc})$ linker, with the only exception of a slightly shorted (by $0.025 \pm 0.006 \text{ \AA}$) for the Pt–Cl distance. For 10PSF sample, we fixed σ_{Cl}^2 to the average value obtained from the two previous fits ($\sigma_{\text{Cl}}^2 = 0.0027 \text{ \AA}^2$) and we optimized N_{Cl} . Table 3 reports the parameters optimized in this refinement procedure.

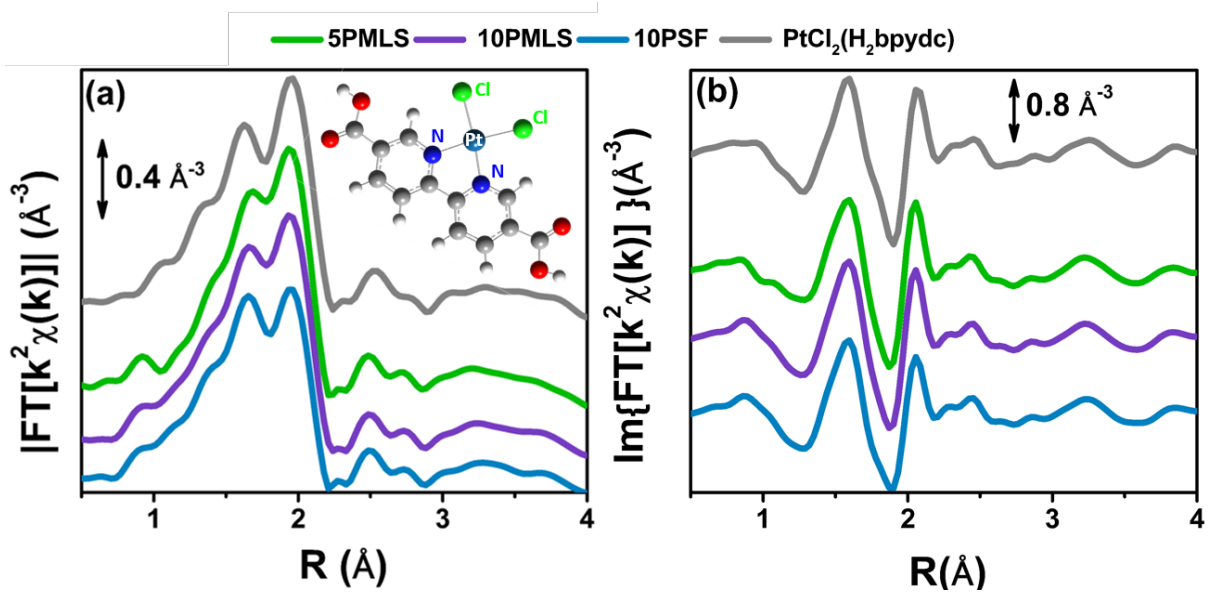


Figure 1. k^2 -weighted, phase uncorrected, modulus (a) and imaginary part (b) of the experimental FT EXAFS spectra for 5PMLS (green), 10PMLS (violet) and 10PSF (cyan) in the as-prepared state at RT in air and the $\text{PtCl}_2(\text{H}_2\text{bpydc})$ (grey) as reference. Spectra were vertically shifted for clarity. The inset in part (a) the $[\text{PtCl}_2(\text{H}_2\text{bpydc})]$ model is also reported, with Pt atom in cyan, N atoms in blue, Cl atoms in green, C atoms in grey, O atoms in red and H atoms in white.

Table 3. Best-fit values of the parameters optimized in the EXAFS fits for the three samples (5PMLS, 10PMLS and 10PSF) in the as-prepared state and for the $\text{PtCl}_2(\text{H}_2\text{bpydc})$ linker model compound. The fits were performed in the R space over the (1.0–4.8) Å interval on $k^2\chi(k)$ function FT-transformed in the (3.1–17.0) Å⁻¹ k -space interval. Fixed parameters are reported by underlined numbers without the corresponding error bars. The quality of the fits can be appreciated in Figure 2.

EXAFS fit parameters	As-prepared (RT, air)			At RT
	5PMLS	10PMLS	10PSF	$\text{PtCl}_2(\text{H}_2\text{bpydc})$ linker
S_0^2	0.94 ± 0.04	0.94 ± 0.04	0.94 ± 0.04	0.93 ± 0.05
ΔE (eV)	0 ± 1	0 ± 1	-1 ± 1	1 ± 1
R -factor	0.016	0.016	0.016	0.018
$N_{\text{par}} (N_{\text{ind}})$	8 (33)	8 (33)	8 (33)	8 (33)
N_{N}	<u>2</u>	<u>2</u>	<u>2</u>	<u>2</u>
$R_{\text{N(bpydc)}} (\text{Å})$	2.008 ± 0.006	2.008 ± 0.006	2.006 ± 0.006	2.01 ± 0.01
$\sigma_{\text{N(bpydc)}}^2 (\text{Å}^2)$	0.0024 ± 0.0005	0.0024 ± 0.0005	0.0020 ± 0.0004	0.0027 ± 0.0006
α_{bpydc}	-0.007 ± 0.004	-0.012 ± 0.004	-0.013 ± 0.004	-0.016 ± 0.005
$\sigma_{\text{bpydc}}^2 (\text{Å}^2)$	0.0016 ± 0.0008	0.002 ± 0.001	0.0024 ± 0.0009	0.0028 ± 0.0015
N_{Cl}	<u>2</u>	<u>2</u>	1.7 ± 0.1	<u>2</u>
$\langle R_{\text{Cl}} \rangle (\text{Å})$	2.281 ± 0.004	2.281 ± 0.004	2.285 ± 0.004	2.306 ± 0.004
$\sigma_{\text{Cl}}^2 (\text{Å}^2)$	0.0026 ± 0.0002	0.0028 ± 0.0002	<u>0.0027</u>	0.0026 ± 0.0004

The EXAFS analysis confirms the satisfactory synthesis for all the investigated samples (5PMLS, 10PMLS and 10PSF), indeed the Pt atom has been successfully grafted the bpydc-linker. For both 5PMLS and 10PMLS samples, Pt(II) ions are coordinated to two Cl ligands, while for the 10PSF samples, around 30% of the Pt(II) species have lost one chlorine ligand in the post synthesis functionalization approach. We can speculate that the coordination vacancy left by such Cl species may be replaced by H species, which are not visible by EXAFS.

Figure 2 shows the experimental modulus and imaginary part of the k^2 -weighted, phase uncorrected, FT of the EXAFS spectra for the as prepared 5PMLS (parts a and b), 10PMLS (parts c and d) and 10PSF (parts e and f), open black circles, compared with the corresponding best fit curves, red lines. The figure also reports the SS contributions of the Cl (green) and N (blue) atoms. We obtained EXAFS fits for all three samples that are, graphically, in very good agreement with the experimental spectra (see Figure 2), as also quantified by R-factor values lower than 2% for all the series of samples, see Table 3.

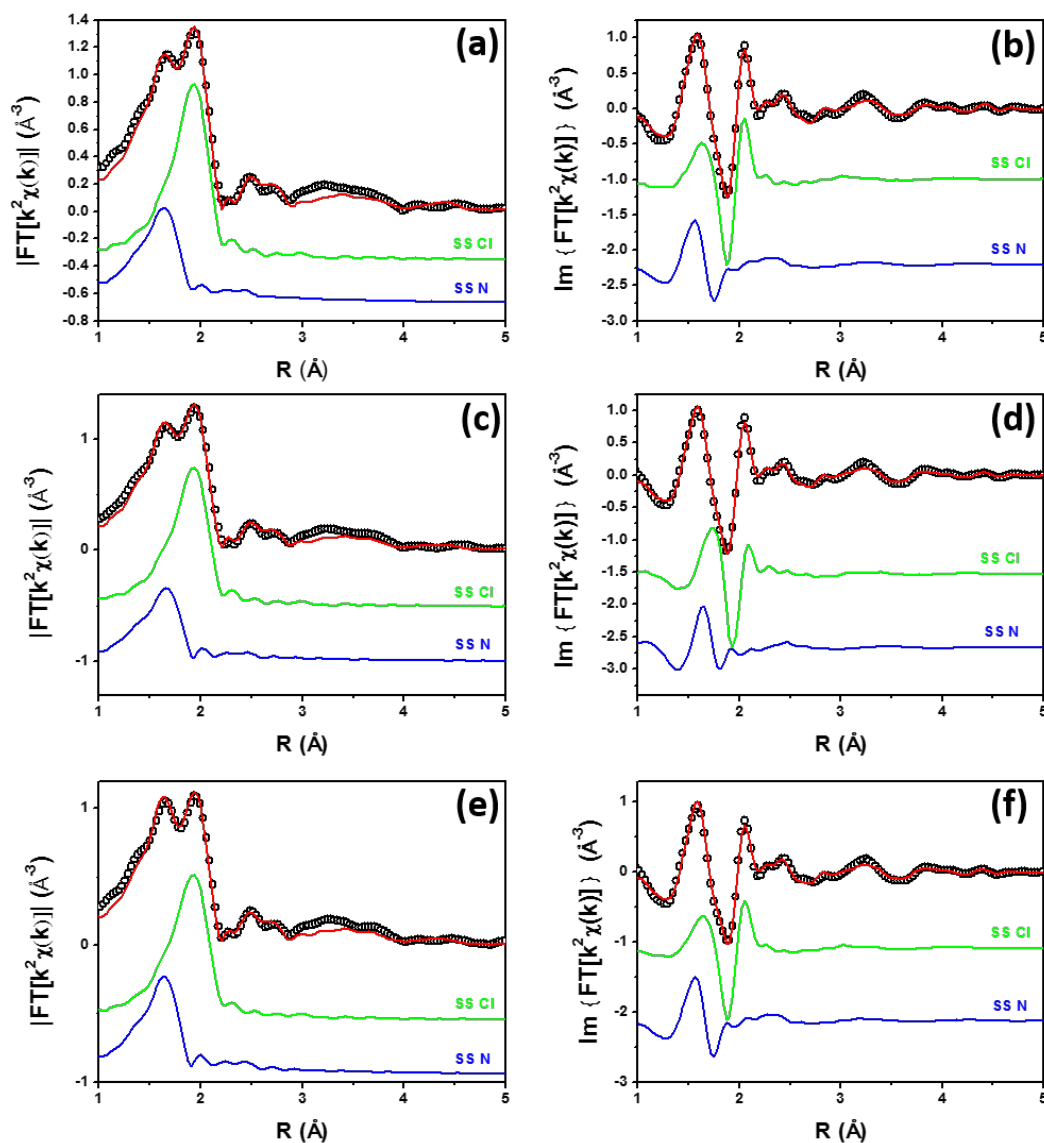


Figure 2. Parts (a,b): k^2 -weighted, phase uncorrected, modulus (a) and imaginary part (b) of the experimental and best fit FT EXAFS spectra for 5PMLS in the as-prepared state (at RT, in air). The experimental data are shown as black open circles and the best fits with red solid lines. The SS contributions involving the N of bpydc (blue), and

Cl (green) atomic neighbours are also reported, vertically translated for the sake of clarity. Parts (c and d) and (e and f) as part (a and b) for 10PMLS and 10PSF respectively. Interval: $\Delta k = 3.1\text{--}17.0 \text{ \AA}^{-1}$ and $\Delta R = 1.0\text{--}4.8 \text{ \AA}$, see Table 3 for the quantitative results of the fits.

3.2. Stability of UiO-67-Pt upon thermal reduction in H_2 : an ex situ XRPD and BET study

The stability of the UiO-67 framework upon thermal reduction in H_2 has been checked by ex situ laboratory XRPD. The diffraction study reported in Figure 3 guarantees that the crystallinity of the three samples is preserved in the reduction treatment (compare gray with black patterns). No reflection from Pt phase could be detected from the gray patterns reported in Figure 3, indicating that the possible formed Pt NPs should be relatively small.

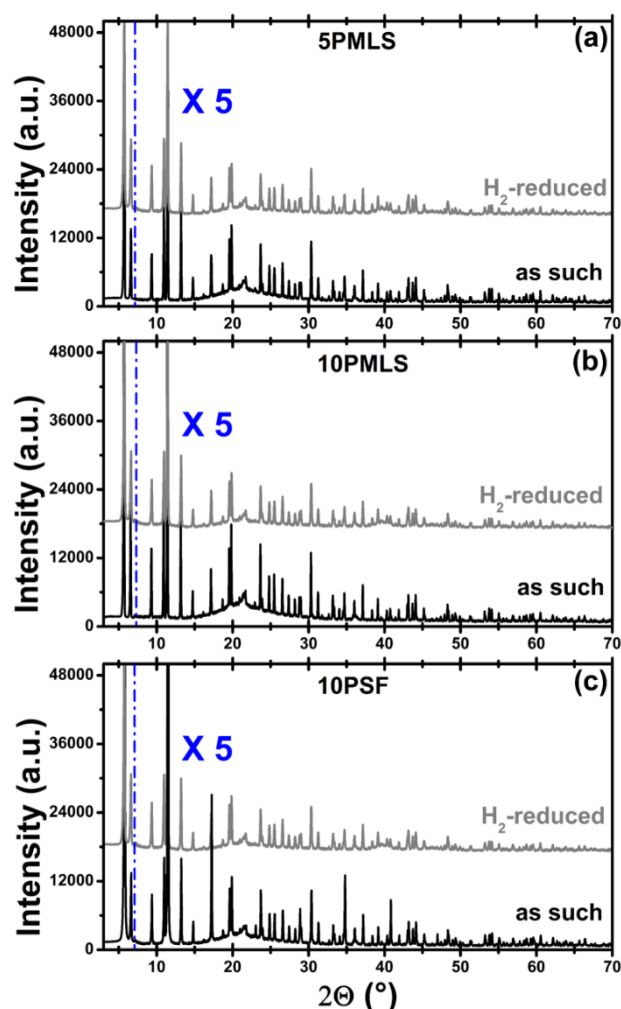


Figure 3. Part (a) XRPD pattern of sample 5PMLS as such at RT (black) and after H_2 -TPR (grey). The broad reflection around $2\theta = 22^\circ$ is due to the window of the cell. Cu $K\alpha$, $\lambda = 1.541 \text{ \AA}$. Patterns were vertically shifted for clarity and the 7-70° region has been multiplied by factor 5 to appreciate the reflection in the high 2θ region. Parts (b) and (c) as part (a) for the 10PMLS and 10PSF samples, respectively.

Conversely, the thermal reduction in H_2 affects, in a different way, both the available surface area and the available pore volume of the three samples as reported in Table 4 from the analysis of the Nitrogen adsorption/desorption isotherms reported in Figure 4. This observation agrees

with the hypothesis of a partial occupation of available pore volume by the formation of Pt NPs. The pore volume decrease is marginal for 10PMLS (−4 %), higher for 10PSF (−9 %) and very consistent for 5PMLS (−29 %), see Table 4. The origin of the different behaviour of the three samples will be understood by the complex EXAFS/TEM analysis described in the following.

It is also worth noticing that the two samples with higher fraction of functionalized bpydc linker (10PMLS and 10PSF) exhibit a lower starting BET area and pore volume compared to 5PMLS, reflecting the partial occupancy of the pore volumes by the bulk $\text{PtCl}_2(\text{bpydc})$ linkers (note that the theoretical surface area of non-functionalized UiO-67 is $2850 \text{ m}^2/\text{g}$ as calculated from grand canonical Monte Carlo method with a probe of radius = 1.82 \AA).⁴⁴

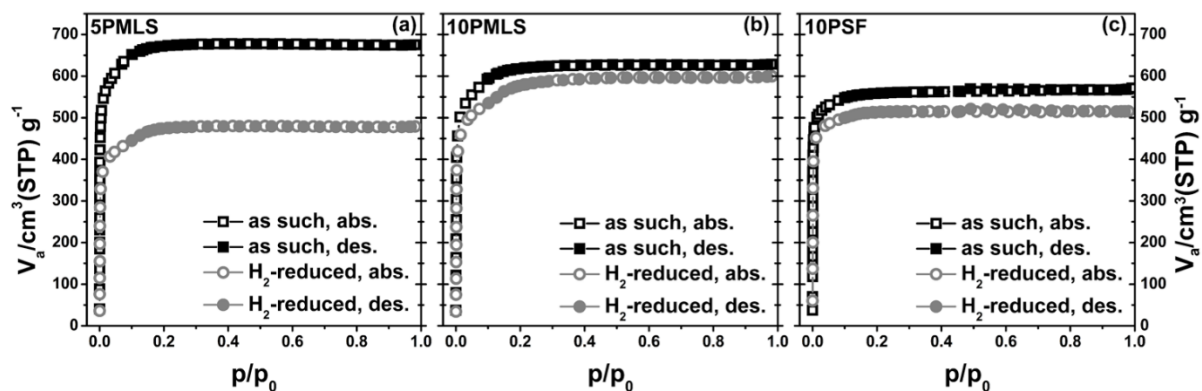


Figure 4. Part (a) Nitrogen adsorption/desorption isotherms for the sample 5PMLS as such (black scatter) and after the H_2 -TPR (grey scatter). Part (b) and (c) as part (a) for the 10PMLS and 10PSF samples, respectively.

Table 4. Surface area and pore volume of fresh and spent 5PMLS, 10PMLS and 10PSF samples. The theoretical surface area of non-functionalized UiO-67 is $2850 \text{ m}^2/\text{g}$ as calculated from grand canonical Monte Carlo method with a probe of radius = 1.82 \AA .⁴⁴

Sample	S_{BET} (m^2/g)	S_{BET} decrease (%)	Total pore volume (cm^3/g)	Total pore decrease (%)
5PMLS	2562		1.04	
5PMLS spent	1766	−31	0.74	−29
10PMLS	2361		0.97	
10PMLS spent	2147	−9	0.93	−4
10PSF	2234		0.88	
10PSF spent	2055	−8	0.80	−9

3.3. Effect of the gas feed on UiO-67-bpydc- PtCl_2 evidenced by quasi-simultaneous XANES and XRPD data collection

The XANES spectra of the as-prepared 10PMLS (violet line) and of the thermally-treated MOF from RT to 623 K in 10% H₂/He, 3% H₂/He and in pure He are reported in Figure 5a and compared to the XANES spectrum of a Pt-metal foil (grey line), employed as a reference for the presence of metallic Pt. When the sample is heated in 10% of H₂/He (green) the XANES spectrum is almost overlapped to Pt metal: indeed the absorption edge slightly shifts towards lower energies, the white line decreases and more defined post-edge features are formed.⁹⁸ Conversely, the spectrum of the sample heated in pure He flow (red line) is fully comparable with what previously observed by us and assigned to isolated Pt sites still grafted to the bpydc linker after the loss of Cl ligands.⁹⁸ In the latter spectrum, the post-edge features are smoother and the white line is slightly more intense with respect to the 10% of H₂/He Pt-UiO-67, but shifted at higher energy. The strong similarity between the XANES shape for the samples treated in H₂ and that of the reference Pt metal foil unambiguously demonstrates that we produced Pt⁰ metal-like species. In addition, also the content of H₂ in the gas feed clearly slightly affects the formation of Pt⁰ clusters as the activation in 3% of H₂/He (orange) results in an intermediate situation.

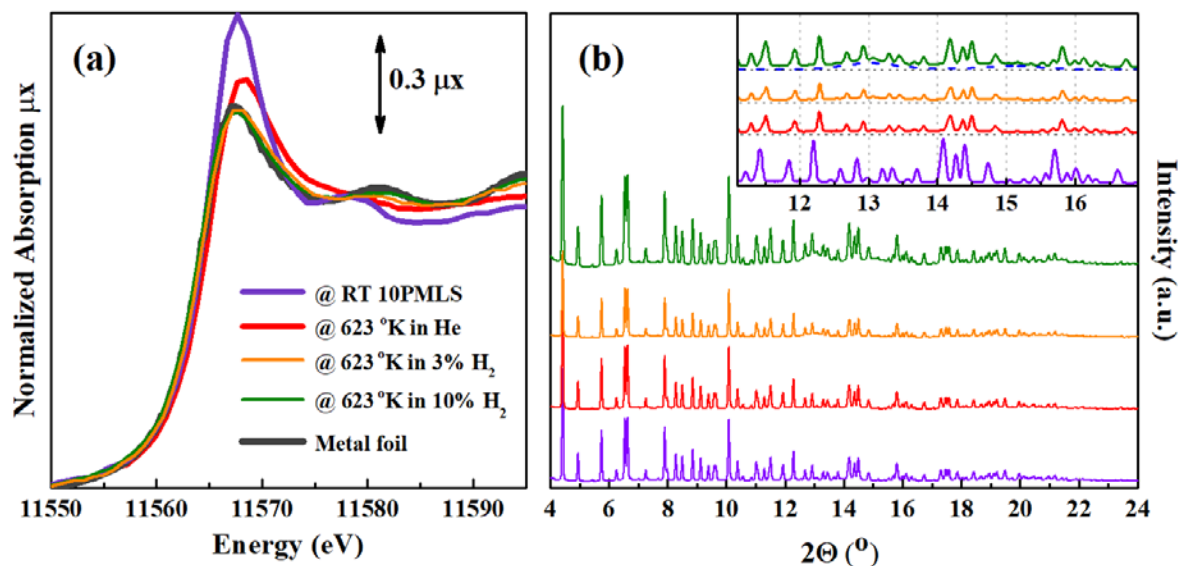


Figure 5. (a) Operando Pt L_{III} edge XANES spectra of as-prepared 10PMLS at RT (violet) and after thermal treatment: in 3% and 10% H₂/He (orange and green, respectively), and in pure He flux (red). The XANES spectrum of the Pt metal foil (grey) is reported as a reference. (b) Operando XRPD patterns taken simultaneously with XANES spectra reported in part (a). $\lambda = 0.51353(1)$ Å. The insert shows the region containing Pt (111) and (200) reflections at 13 and 15 ° in 2θ , respectively. The blue dashed curve represents the simulated scattering signal for the 2.3 nm Pt nanoparticle with cell parameter $d = 3.92$ Å. The same experiments repeated for 5PMLS and 10PSF samples resulted in an equivalent behavior.

The picture obtained from the XANES study is supported by the quasi-simultaneous XRPD data collection, Figure 5b. The operando XRPD study, besides confirming the stability of the UiO-67 framework (already proven in the *ex situ* study reported in Figure 3), allows to detect for the sample reduced in 10% H₂ the broad (111) and (200) reflections of the Pt metal phase at 13 and 15 ° in 2θ , respectively. Such reflection are better visible in the inset (dashed blue lines).

Cell parameters and the FWHM of UiO-67 (333) reflection are summarized in the Table 5. The decrease of the cell parameter during the activation is caused by dehydration process. The increase of FWHM for the 10% H₂ activated sample may be due to the distortions in the UiO-67 structure induced by particle formation.

Table 5. Summary of the Rietveld refinements of the XRPD patterns reported in **Figure 5b**

Sample conditions	as such	After He activation	After activation in 3% H ₂	After activation in 10% H ₂
cell parameter (Å)	26.831(3)	26.636(2)	26.626(3)	26.642(4)
2θ FWHM (333) (°)	0.060	0.049	0.048	0.061

3.4. Determination of the Pt local environments in UiO-67-Pt after H₂-TPR by static EXAFS.

The samples were heated up to 623 K in 10% H₂/He, while collecting *operando* XAS (XANES and EXAFS) spectra to monitor the evolution of electronic and structural properties of Pt-sites during TPR. *Operando* XANES spectra are reported in Figure 6a for the 10PMLS sample. The XANES spectrum for the as-prepared material (red spectrum in Figure 6a) is characterized by the absence of any defined pre-edge/edge peaks, and by a rather intense white line feature at ~11560 eV. While increasing the temperature during TPR, clear modifications occur in the XANES spectra, including a progressive reduction of the white line intensity and the evolution of more structured post-edge features at ~11575 eV and at ~11590 eV, well evident in the final spectrum at 623 K (black spectrum in Figure 6a). As anticipated in Section 3.1, this shape of the XANES spectrum matches the spectrum of the Pt-metal foil. This evidence is further supported by the evolution of the k²-weighted, phase uncorrected FT of the corresponding EXAFS curves (Figure 6b). The same behaviour has been observed in the XANES and EXAFS spectra of 5PMLS and 10PSF samples, as shown in Figure S3 in the ESI.

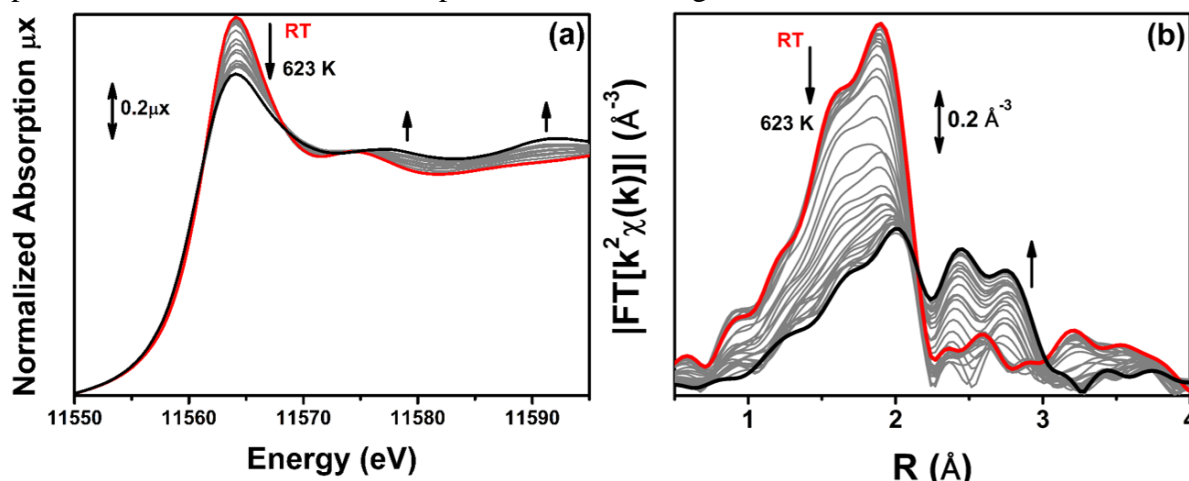


Figure 6. Part (a): Sequence of Pt L_{III} edge *operando* XANES spectra of 10PMLS during TPR, collected at the starting point at RT (red) and upon heating to 623 K in 10% H₂/He (grey) until the steady state at 623 K is reached (black). Part (b): as part (a) for the k²-weighted, phase uncorrected FT of the corresponding EXAFS curves

When the XANES spectra collected at 623 K demonstrated no further time-dependent changes, we have cooled down the sample to RT for high-quality EXAFS data collection. Figure 7 compares the modulus and the imaginary part of the FT of the EXAFS spectra for 10PMLS in the initial state (as-prepared material, at RT before TPR, red curves) and in the final state, after TPR and subsequent cooling at RT (orange curves). For comparison, Figure 7 also reports the corresponding spectra of Pt-metal foil (grey curves). The same EXAFS spectra of 5PMLS and 10PSF samples are shown in Figure S4. After activation, the modulus is characterized by four significant contributions centred around 1.7 Å, 1.9 Å, 2.2 Å and 2.6 Å (Figure 7a). The first two peaks, as already discussed in Section 3.1, are associated with the Pt–N and Pt–Cl SS paths, respectively, and are in phase with signals present in the red spectrum. The two maxima at 2.2 Å and 2.6 Å correspond both to the SS of a single Pt–Pt contribution of Pt metal (a double-shaped modulus of the FT is typical of a single distance in EXAFS when the scattering atom is a high Z one such as e.g. Ag¹⁵³, In¹⁵⁴ or Pt⁹²).

During the thermal treatment, the signals from Pt–N and Pt–Cl coordination shells decrease while the peaks at 2.2 Å and 2.6 Å rise, see Figure 6b. This is an evidence of the nucleation of the Pt⁰ metal nanoparticles (NPs), formed after the progressive detachment of the Pt framework atoms. It is worth to note that even if the intensity of the Pt–Cl contribution is drastically diminished with respect to the as-prepared material, there is still a significant residual signal of Pt–Cl.

The formation of Pt NPs is further supported by TEM analysis on the three UiO-67-Pt samples. TEM shows that NPs are produced after the TPR for the all samples' series. Figure 8 presents the distribution of particle size (parts (a), (d) and (g)) weighted by the number (blue bars) and by the volume (green bars) of the particles^{92, 155} and the TEM microscopy images at low (parts (b), (e), (h)) and at high (parts (c), (f) and (i)) magnification. In all the samples, Pt NPs are well dispersed in the MOF matrix and no evidence of NP aggregation has been observed.

The size particle distribution (blue histograms in Figure 8a,d,g), $w_P(d_i)$, provides the fraction w_P of NP having a diameter d in the interval $[d_i - \varepsilon < d \leq d_i + \varepsilon]$, being $\varepsilon = 0.25$ nm in the adopted cases. From our study, it emerges that $w_P(d_i)$ depends on the Pt loading and on the synthesis method. Between samples prepared with the PMLS approach, an average smaller size is obtained with the sample with lower Pt loading: $\langle d \rangle = (2.6 \pm 0.8)$ nm vs. (3.5 ± 1.2) nm, for 5PMLS and 10PMLS, respectively. Comparison of the samples with the same loading demonstrates that the PMLS method is more efficient in keeping a low particle size than the PSF, being $\langle d \rangle = (4.4 \pm 2.4)$ nm for 10PSF. All reported $\langle d \rangle$ values refer to the particle distribution weighted by number of particles (blue distributions in Figure 8a,d,g, usually reported in the TEM studies). When the same distributions are weighted by the volume, 10PSF clearly exhibit bimodal distribution. As all Pt atoms contribute to the EXAFS signal, a large particle has a greater weight in the overall EXAFS signal than a small one. For this reason, when EXAFS and TEM studies are compared, the relevant size distribution is the volume-weighted one ($w_V(d_i)$, green histograms in Figure 8a,d,g),^{92, 155} that is obtained from the particle weighted one according to Eq. (2):

$$w_V(d_i) = \frac{4\pi}{3V} \left(\frac{1}{2} d_i\right)^3 w_P(d_i), \text{ where: } V = \sum_{i=1}^n \frac{4\pi}{3} \left(\frac{1}{2} d_i\right)^3 w_P(d_i). \quad (2)$$

Once the shape of a NP is known (e.g. from the TEM study) the average coordination number of a given fcc NP is unambiguously given by its diameter, $N(d_i)$.^{156, 157} Successively, using the $w_V(d_i)$ distribution it is possible to estimate the average coordination number of the whole particle distribution (N_{Pt}) as:

$$N_{Pt} = \sum_{i=1}^n N(d_i)w_V(d_i) \quad (3)$$

The values of N_{Pt} for the three samples are given in Table 6.

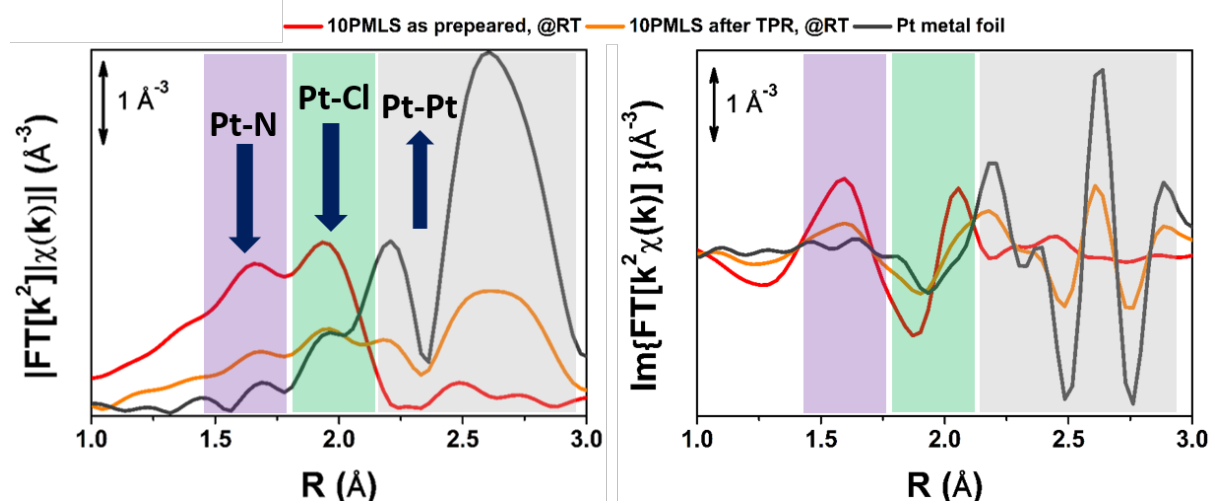


Figure 7. k^2 -weighted, phase uncorrected, modulus (a) and imaginary part (b) of the experimental FT EXAFS spectra for 10PMLS in the as-prepared state at RT in air (red) and after TPR up to 623 K in 10% H_2/He and subsequent cooling to RT (orange). The corresponding spectra of the Pt-metal foil are also reported (grey) for comparison.

Quantitative analysis of the EXAFS spectra collected at RT after the thermal treatment was performed assuming the presence of the [bpydc- $PtCl_2$] linker component, already used to fit the spectra of the as-prepared materials, and the Pt^0 metal cluster component, with fixed N_{Pt} .

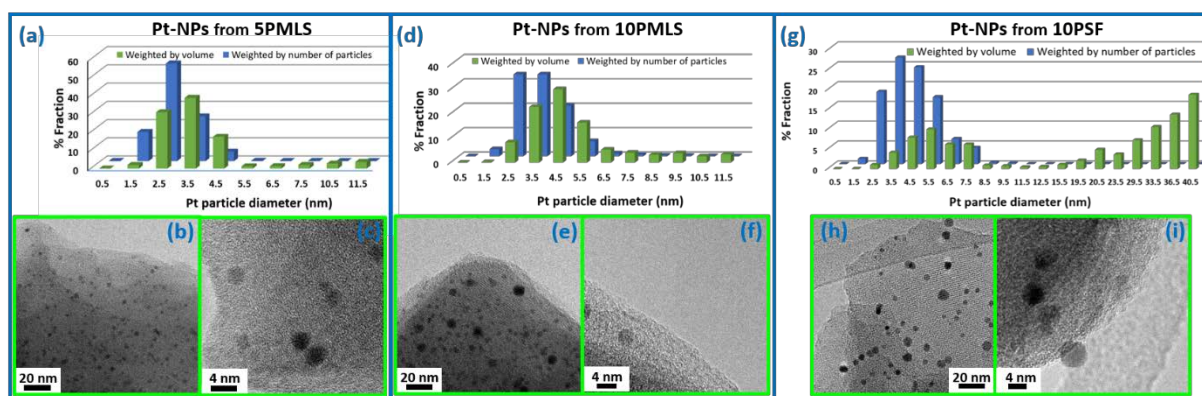


Figure 8. (a) Particle size distribution weighted by number (blue) and by volume (green) of Pt-NPs for the 5PMLS sample after TPR in 10% H_2/He . (b) and (c) report representative TEM images collected at 100000 \times and 500000 \times of magnification, respectively, for the 5PMLS sample. Parts (d, e and f) and (g, h and i) as part (a, b and c) for 10PMLS and 10PSF, respectively. The total number of counted particles are: 1545 for 5PMLS, 2135 for 10PMLS and 1259 for 10PSF.

The assumption of the coexistence of two structural components increases significantly the number of variables that must be taken into account in the EXAFS analysis. The contribution of the two phases in the EXAFS fit has been distinguished multiplying the amplitude of the EXAFS equation for the metal Pt⁰ phase by a free variable x , representing the content of Pt-NPs, and the linker phase by a factor $(1-x)$. In this manner, the concentration of Pt-NPs formed can be figured out. The fit has been performed in the ΔR range of (1.0–3.1) Å, defined considering the first coordination shell of the Pt-metal phase.

To achieve a reliable EXAFS fit on a so complex system, we had set a series of selected parameters based on the analysis of two pure phases: as-prepared materials (Table 3 and Figure 2) and reference Pt-metal foil (Table S1 and Figure S5). All parameters of the isolate framework Pt phase have been fixed to the values optimized in Table 3, with the only exception of the N_{Cl} coordination number. Indeed, along the TPR treatment, a fraction of the Pt atoms remained anchored to the MOF framework may have lost one or two Cl ligands. It should be noted that the Pt-NPs formation is not immediate, but it should evolve through several intermediate steps such as [bpydc-Pt(II)Cl][−], [bpydc-Pt(II)]^{2−}, [bpydc-Pt⁰] etc., along the reaction paths to Pt-NPs. Indeed, considering the spectrochemical series, it is energetically favourable breaking firstly the Pt–Cl bond with respect to the Pt–N one to bpydc;¹⁵⁸ this behaviour is also supported by our previous EXAFS results.⁹⁸

Concerning the Pt-NP phase, the only optimized parameters were σ^2_{Pt} and R_{Pt-Pt} , which can differ significantly comparing bulk Pt⁰ and Pt-NPs. As for the first shell Pt–Pt coordination number, N_{Pt} , it was fixed based on TEM results that allows us to obtain the average N_{Pt} based on the volume-weighted particle size distribution reported in Figure 8a,d,g,^{92, 155, 157, 159, 160} assuming a spherical shape for the Pt-NPs.

The results of the EXAFS analysis of the three samples after the TPR are reported in Table 6, while the quality of the fit can be appreciated in Figure 9. The agreement between experimental (open black circles) and theoretical (red lines) curves is remarkable for a so complex system, taking into account that the model uses only 4 free parameters (x , N_{Cl} , σ^2_{Pt} and R_{Pt-Pt}). Such a result can be obtained only if the constraints used for all the non-optimized parameters have been properly set.

Table 6. Best-fit values of the parameters optimized in the EXAFS fits for the three samples (5PMLS, 10PMLS and 10PSF) after TPR in 10% H₂/He-flow at 623 K (data collected at RT). The fits were performed in the k-space interval $\Delta k = (3.1–17.0)$ Å^{−1} and R-space interval $\Delta R = (1.0–3.1)$ Å. The underlined parameters were fixed in the fit and have no associated error.

EXAFS fit parameters	After TPR (RT-623K) in 10% H ₂ /He		
	5PMLS	10PMLS	10PSF
S_0^2 (bpydc-PtCl ₂)	<u>0.94</u>	<u>0.94</u>	<u>0.94</u>
S_0^2 (Pt ⁰ metal)	<u>0.83</u>	<u>0.83</u>	<u>0.83</u>
ΔE (Pt-linker) (eV)	<u>10</u>	<u>10</u>	<u>9</u>
ΔE (Pt ⁰ metal) (eV)	<u>7.3</u>	<u>7.3</u>	<u>7.3</u>

Fraction of Metal (%)	53 ± 2	61 ± 2	43 ± 2
R -factor	0.008	0.007	0.01
N_{par} (N_{ind})	4 (18)	4 (18)	4 (18)
$\langle R_{\text{N(bpydc)}} \rangle$ (\AA)	<u>2.005</u>	<u>2.007</u>	<u>2</u>
$\sigma^2_{\text{N(bpydc)}}$ (\AA^2)	<u>0.0029</u>	<u>0.0024</u>	<u>0.0020</u>
N_N	<u>2</u>	<u>2</u>	<u>2</u>
α_{bpydc}	<u>-0.008</u>	<u>-0.012</u>	<u>-0.015</u>
σ^2_{bpydc} (\AA^2)	<u>0.002</u>	<u>0.002</u>	<u>0.002</u>
$\langle R_{\text{Cl}} \rangle$ (\AA)	<u>2.281</u>	<u>2.281</u>	<u>2.284</u>
σ^2_{Cl} (\AA^2)	<u>0.0029</u>	<u>0.0028</u>	<u>0.0035</u>
N_{Cl}	1.5 ± 0.1	1.3 ± 0.1	1.3 ± 0.1
R_{Pt} (\AA)	2.756 ± 0.004	2.754 ± 0.003	2.756 ± 0.003
σ^2_{Pt} (\AA^2)	0.0064 ± 0.0002	0.0062 ± 0.0002	0.0064 ± 0.0002
N_{Pt}	<u>10.51</u>	<u>10.89</u>	<u>11.95</u>

EXAFS analysis revealed that, at the end of the TPR run, the Pt-MOFs synthesized by PMLS method produces more Pt-NPs than the PSF. Indeed, 5PMLS and 10PMLS yielded the 53% and 61% of Pt-NPs compared to the 43% obtained for 10PSF. The σ^2_{Pt} for the formed Pt-NPs, $(0.0064 \pm 0.0002) \text{\AA}^2$, is higher than the value derived from the analysis of bulk Pt metal, $\sigma^2_{\text{Pt(foil)}} = (0.0047 \pm 0.0001) \text{\AA}^2$, as expected due to the higher structural disorder in the Pt-NPs phase formed during TPR. Also the Pt–Pt distance undergoes a small contraction with respect to the bulk value of about 0.01\AA , in agreement with what reported in the literature.¹⁶¹⁻¹⁶³

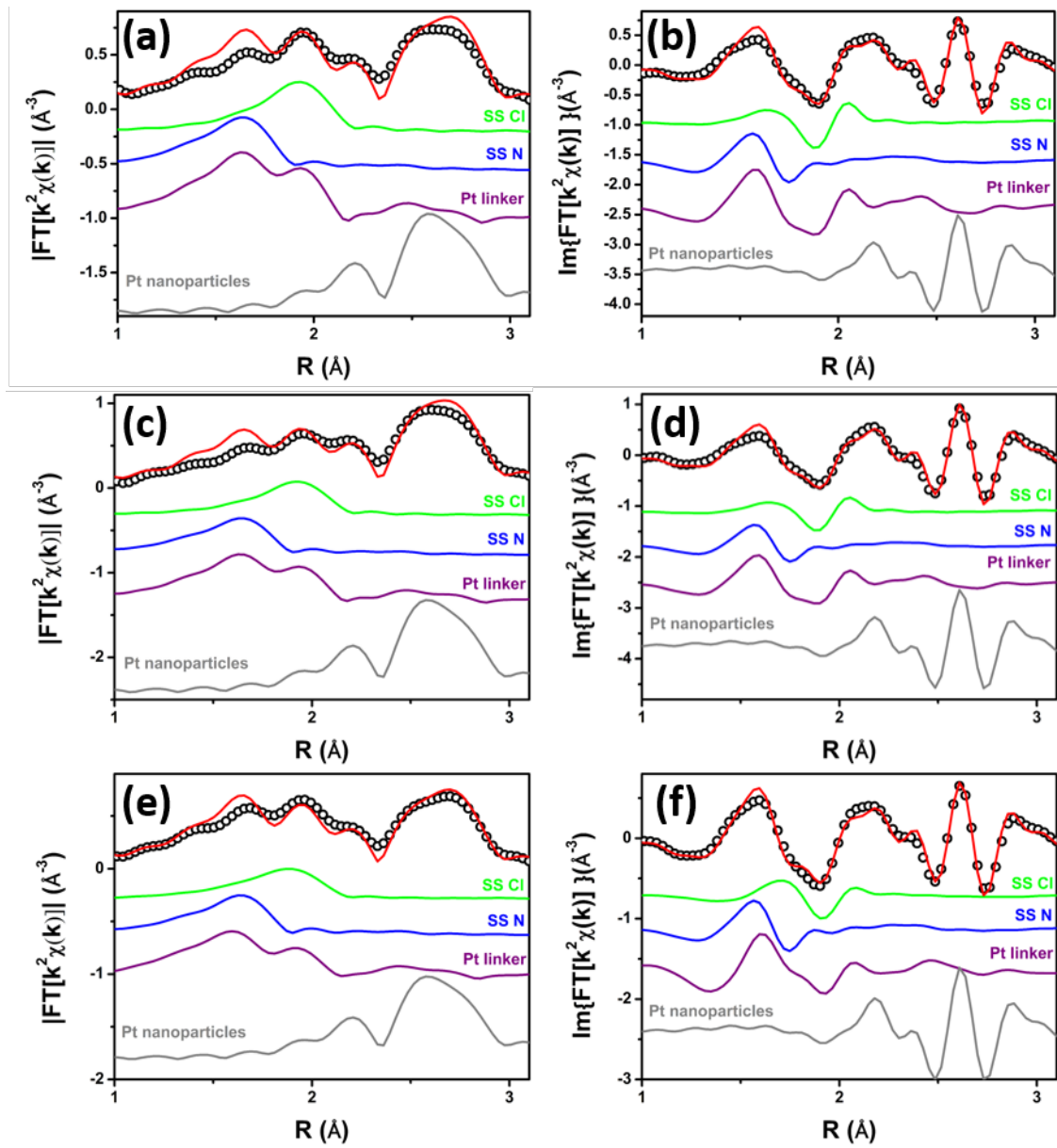


Figure 9. Parts (a,b): k^2 -weighted, phase uncorrected, modulus (a) and imaginary part (b) of the experimental and best fit FT EXAFS spectra for 5PMLS in static condition at 623K in 10% H_2 /He. The experimental data are shown as black dots and the best fit with red solid line. Moreover, the SS contributions involving the N of bpydc (blue), and Cl (green) atomic neighbours as well as the sum of SS and MS involving Pt linker (violet) and the Pt-NPs (grey) contributions are reported. Parts (c and d) and (e and f) as part (a and b) for the 10PMLS and 10PSF respectively.

3.5. Determination of the evolution Pt local environment in UiO-67-Pt along TPR by operando EXAFS.

The EXAFS analysis of the spectra collected under *operando* conditions along the TPR experiment has followed the complex four-step procedure described in detail in Section 2.5. The results are summarized in Figure 10 for the three samples. We selected the first-shell Pt–Pt SS path as an indicator for Pt-NPs formation, whereas the Pt–N(bpydc) and Pt–Cl SS paths are representative for the Pt-linker component. Figure 10 shows the time-dependent behaviour of

the $N_i \cdot x_i \cdot S_0^2$ product between the coordination number N_i , the relative fraction x_i and by the scattering amplitude factor S_0^2 , with i indicating the three Pt atomic neighbours considered, i.e. N, Cl and Pt. In the TPR-EXAFS analysis is not possible to quantify the absolute content of Pt-NPs, because both particle size (and thus the average N_{Pt}) and particle fraction (x) increase along the experiment and a TEM study, as we had for the final sample, for the intermediate steps during TPR would be extremely challenging and beyond the scope of the present work. Notwithstanding this limitation, it is meaningful to observe the comparison of the relative weight of Pt–Pt contribution with respect to the Pt–Cl and Pt–N ones during the TPR. Moreover, the Pt–Cl and Pt–N contributions decrease significantly at 623 K, and with the same trend.

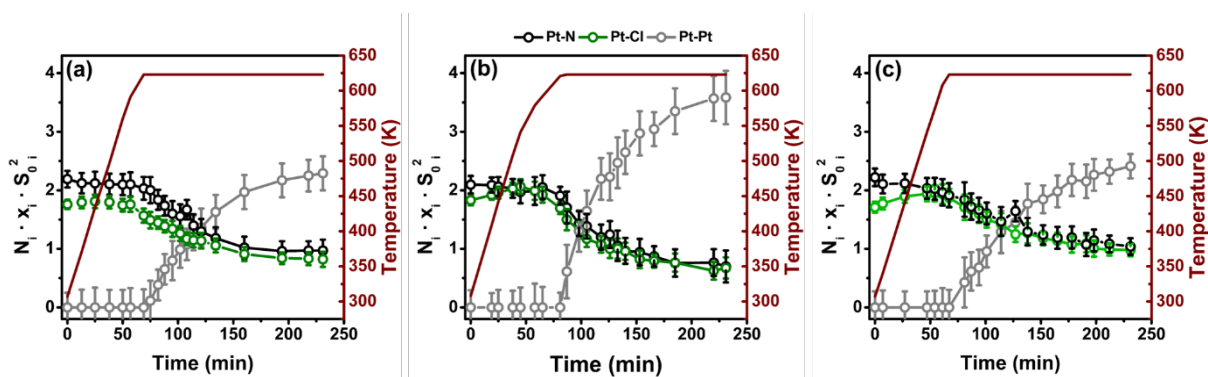


Figure 10. (a) Results of the simultaneous parametric analysis of *operando* EXAFS collected during TPR for 5PMLS. The amplitude factor reported in the Figure as a function of time is defined by the product between the coordination number N_i , the relative fraction x_i and by the scattering amplitude factor S_0^2 , where i denote the three kind of SS considered, i.e. Pt–N and Pt–Cl for the Pt-linker component, and Pt–Pt for the Pt-NPs phase (N in black, Cl in green and Pt in grey). Parts (b) and (c) as part (a) for the 10PMLS and 10PSF respectively.

Data analysis reveals that sample synthesized with the PSF method, which starts from an initial situation with less Cl, is less prone to form Pt-NPs than the samples synthesized with PMLS method.

3.6. Determination of the Pt-NPs concentrations with LC and a linear combination of XANES spectra approach supported by PCA analysis

The operando XANES spectra collected during H₂-TPR have been analysed using the principal component analysis (PCA) with Fitit software¹⁶⁴ and the linear combination analysis (LCA) with the Athena software.¹³⁰ In the absence of experimental error, PCA will lead the exact numbers of abstract meaningful components, *i.e.* the exact dimension of the experimental dataset. Unfortunately, perfect data are not attainable and noise unavoidably produces a number of extra-components whose retention leads, clearly, to the complete reproduction of the entire dataset, including experimental errors.¹⁶⁵ For this reason a series of statistical estimators are used in order to deduce the correct number of principal components (PCs).¹⁶⁵⁻¹⁶⁷ One of them is the so called Malinowski indicator factor (IND). It consists of an empirical function that reaches a minimum in presence of the correct number of components making possible to drastically reduce the experimental error contributes in the data reproduction. Based on the imbedded error (IE) and the IND¹⁶⁸ (Figure 6), PCA has revealed five components for all the

UiO-67-Pt samples. However, recent articles showed that this method can sometimes fail.¹⁶⁹⁻¹⁷¹ In particular IND performance critically depends on the amount of noise in the data and may result in considerable overestimation of the number of components, moreover the accuracy of the component recovery seems to depend on the size of the dataset.¹⁷¹ For these reasons in our LC reconstruction, we considered only the first two main components which are predominant over less important data features (*i.e.* intermediates of reactions) and noise, as described in Figure S7 of the ESI. Being primarily interested in tracking the Pt-NPs formation during the TPR, we adopted a quick and informative method as LCA, widely used to analyse series of time evolving XANES spectra.^{122, 172-174} We have selected as references for operando XANES LCA only the two key-species present in the whole sample series, *i.e.* Pt⁰ metal sites (Pt-metal foil XANES spectrum) and (PtCl₂)bpdc complexes (RT spectra collected before the TPR). The R-factors obtained for LCA are in the order of the 10⁻⁵ for each spectrum, meaning that the employed references are able to provide an adequate reproduction of the experimental spectra, although possible Cl-deficient Pt-linker species are not included in LCA. Figure 11 reports the result of the linear combination analysis showing the behaviour of the Pt-NPs component as a function of time and temperature for the 5PMLS (green), 10PMLS (violet) and 10PSF (cyan). Noteworthy, the Pt-NPs concentration increases slightly for all the samples until the temperature of 623 K is reached. At 623 K there is a sudden increase in the growth rate of Pt-NPs, which reaches a plateau after almost 4h at constant temperature. The same exponential behaviour has been observed for the different samples, although the absolute values of Pt-NPs is formed. Indeed, the MOF synthesized by PMLS method, as already seen in EXAFS analysis, yields more Pt-NPs than the PSF method. In Table 6 are reported the Pt-NPs concentration values when the temperature of 623 K is just reached, after 1h, ca. 4h at constant temperature and, finally, at RT after TPR. The values derived with EXAFS and LCA after TPR are equivalent within their respective errors.

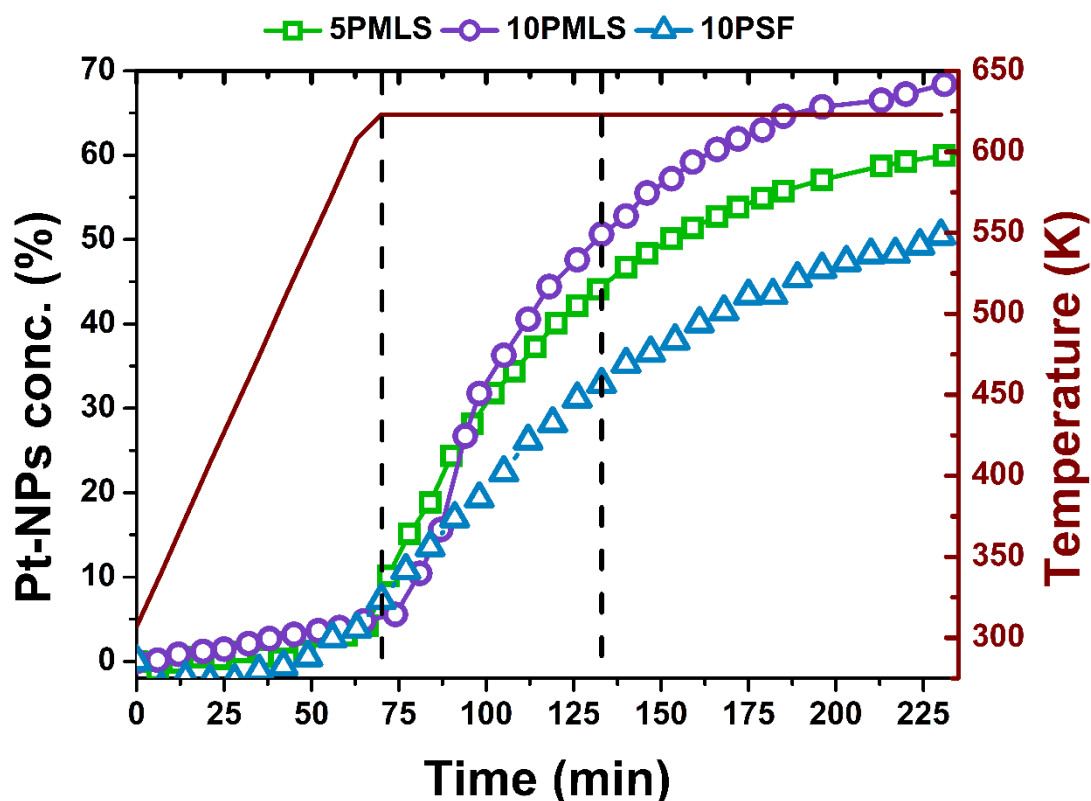


Figure 11. Evolution of Pt-NPs percentage concentration depending on time and on temperature (burgundy colour, reported also on y-axis) for the 5PMLS (green), 10PMLS (violet) and 10PSF (cyan). The first black vertical line represents the reaching of 623 K and the second vertical line is after 1h at constant temperature.

Table 7. Values of Pt-NPs concentration (%) as derived from the linear combination analysis (LCA) and TPR-EXAFS at different time/temperature points for 5PMLS, 10PMLS and 10PSF.

Sample	From XANES LCA analysis				From EXAFS, see Table 6
	Pt-NPs(%) at 623K (0 h)	Pt-NPs(%) at 623K (after 1 h)	Pt-NPs(%) at 623K (after 4 h)	Pt-NPs(%) after cooling at RT	Pt-NPs(%) at RT
5PMLS	4 ± 1	44 ± 2	59 ± 2	57 ± 3	53 ± 2
10PMLS	10 ± 1	57 ± 2	68 ± 2	61 ± 1	61 ± 2
10PSF	11 ± 1	35 ± 2	49 ± 2	48 ± 2	43 ± 2

4. Conclusions

In this work, we demonstrate the successful Pt-functionalization UiO-67 MOF with two different synthesis methods (PMLS and PSF) and Pt loading (2.8 and 5.5% wt.). In addition, it has been shown, by means of XANES, that functionalized MOFs are sensitive to gas feed during temperature activation (from RT to 623K): (i) in pure He the Cl ligands are lost but Pt site remains grafted to the linker, while (ii) in H₂ Pt-NPs are formed. The formation of Pt-NPs has been followed during TPR with *operando* EXAFS in H₂/He flow, successively analyzed with a parametric approach based on the Einstein model to minimize the correlation among optimized parameters. A simultaneous loss of Cl and N ligands has been observed under

isothermal conditions once 623 K was reached. The TEM analysis of the recovered sample revealed that NPs were produced during the TPR treatment for the whole set of samples. We found that the size distribution of the NPs depends on the Pt loading and on the synthesis method. Samples prepared with the PMLS approach present an average smaller for the sample with lower Pt loading: $\langle d \rangle = (2.6 \pm 0.8)$ nm vs. (3.5 ± 1.2) nm, for 5PMLS and 10PMLS, respectively. While the samples with the same Pt loading demonstrates that the PMLS method is more apt to keep a low particle size then the PSF, being $\langle d \rangle = (4.4 \pm 2.4)$ nm for 10PSF. The particle size distribution obtained from the TEM study allowed us to fix the Pt-Pt coordination number and to perform a complex EXAFS data analysis on the samples at the end of the TPR experiment allowing to quantitatively determine the fraction of Pt atoms in the NP phase to be: 53, 61 and 43 % for 5PMLS, 10PMLS and 10PSF respectively. These values have been quantitatively confirmed by linear combination analysis of the XANES spectra. *Operando* XANES experiments were supported by quasi simultaneous X-ray powder diffraction (XRPD) data collection testifying the resistance of the UiO-67 framework to TPR. *In situ* XANES/EXAFS study were supported by *ex-situ* XRPD and BET analyses, confirming the framework stability and testifying a loss of the internal volume after TPR due to the formation of Pt NPs insides the MOF pores, more relevant in the sample where smaller Pt NPs were formed.

Acknowledgments

We are indebted to S. Bordiga (University of Turin) for having taken part to the experiments in Lund and for fruitful discussion. LB, KAL, ALB, AAG, AVS and CL acknowledge the Megagrant of the Russian Federation Government to support scientific research at the Southern Federal University, no. 14.Y26.31.0001. Authors are grateful to MAX-lab for the allocation of the beam time (proposal 20140449) and to Dr. Stefan Carlson for the technical support during the experiments at the I811 beamline. We also acknowledge the whole SNBL staff for their precious help during the experiments at the ESRF.

Notes and references

1. G. Ferey, *Chem. Mat.*, 2001, **13**, 3084-3098.
2. S. L. James, *Chem. Soc. Rev.*, 2003, **32**, 276-288.
3. J. J. Perry, J. A. Perman and M. J. Zaworotko, *Chem. Soc. Rev.*, 2009, **38**, 1400-1417.
4. D. J. Tranchemontagne, J. L. Mendoza-Cortes, M. O'Keeffe and O. M. Yaghi, *Chem. Soc. Rev.*, 2009, **38**, 1257-1283.
5. S. T. Meek, J. A. Greathouse and M. D. Allendorf, *Adv. Mater.*, 2011, **23**, 249-267.
6. D. Zhao, D. J. Timmons, D. Q. Yuan and H. C. Zhou, *Accounts Chem. Res.*, 2011, **44**, 123-133.
7. M. O'Keeffe and O. M. Yaghi, *Chem. Rev.*, 2012, **112**, 675-702.
8. N. Stock and S. Biswas, *Chem. Rev.*, 2012, **112**, 933-969.
9. T. R. Cook, Y. R. Zheng and P. J. Stang, *Chem. Rev.*, 2013, **113**, 734-777.
10. H. Furukawa, K. E. Cordova, M. O'Keeffe and O. M. Yaghi, *Science*, 2013, **341**, Pag. 974; Art. n. 1230444.
11. T. H. Chen, I. Popov, W. Kaveevivitchai and O. S. Miljanic, *Chem. Mater.*, 2014, **26**, 4322-4325.
12. V. V. Butova, M. A. Soldatov, A. A. Guda, K. A. Lomachenko and C. Lamberti, *Russ. Chem. Rev.*, 2016, **85**, doi: 10.1070/rcr4554.
13. Y. J. Cui, B. Li, H. J. He, W. Zhou, B. L. Chen and G. D. Qian, *Accounts Chem. Res.*, 2016, **49**, 483-493.
14. A. Schoedel, M. Li, D. Li, M. O'Keeffe and O. M. Yaghi, *Chem. Rev.*, 2016, **116**, 12466-12535.
15. T. L. Easun, F. Moreau, Y. Yan, S. H. Yang and M. Schroder, *Chem. Soc. Rev.*, 2017, **46**, 239-274.
16. Q. G. Zhai, X. H. Bu, X. Zhao, D. S. Li and P. Y. Feng, *Accounts Chem. Res.*, 2017, **50**, 407-417.

17. A. J. Howarth, A. W. Peters, N. A. Vermeulen, T. C. Wang, J. T. Hupp and O. K. Farha, *Chem. Mater.*, 2017, **29**, 26-39.
18. J. Lee, O. K. Farha, J. Roberts, K. A. Scheidt, S. T. Nguyen and J. T. Hupp, *Chem. Soc. Rev.*, 2009, **38**, 1450-1459.
19. L. Ma, C. Abney and W. Lin, *Chem. Soc. Rev.*, 2009, **38**, 1248-1256.
20. M. Yoon, R. Srirambalaji and K. Kim, *Chem. Rev.*, 2012, **112**, 1196-1231.
21. K. Lillerud, U. Olsbye and M. Tilset, *Top. Catal.*, 2010, **53**, 859-868.
22. A. Corma, M. Iglesias, F. Xamena and F. Sanchez, *Chem.-Eur. J.*, 2010, **16**, 9789-9795.
23. C. Prestipino, L. Regli, J. G. Vitillo, F. Bonino, A. Damin, C. Lamberti, A. Zecchina, P. L. Solari, K. O. Kongshaug and S. Bordiga, *Chem. Mater.*, 2006, **18**, 1337-1346.
24. E. Borfecchia, S. Maurelli, D. Gianolio, E. Groppo, M. Chiesa, F. Bonino and C. Lamberti, *J. Phys. Chem. C*, 2012, **116**, 19839-19850.
25. F. Bonino, S. Chavan, J. G. Vitillo, E. Groppo, G. Agostini, C. Lamberti, P. D. C. Dietzel, C. Prestipino and S. Bordiga, *Chem. Mater.*, 2008, **20**, 4957-4968.
26. S. Chavan, J. G. Vitillo, E. Groppo, F. Bonino, C. Lamberti, P. D. C. Dietzel and S. Bordiga, *J. Phys. Chem. C*, 2009, **113**, 3292-3299.
27. S. Chavan, F. Bonino, L. Valenzano, B. Civalieri, C. Lamberti, N. Acerbi, J. H. Cavka, M. Leistner and S. Bordiga, *J. Phys. Chem. C*, 2013, **117**, 15615-15622.
28. S. L. Qiu and G. S. Zhu, *Coord. Chem. Rev.*, 2009, **253**, 2891-2911.
29. Z. Wang and S. M. Cohen, *Chem. Soc. Rev.*, 2009, **38**, 1315-1329.
30. H. X. Deng, C. J. Doonan, H. Furukawa, R. B. Ferreira, J. Towne, C. B. Knobler, B. Wang and O. M. Yaghi, *Science*, 2010, **327**, 846-850.
31. B. L. Chen, S. C. Xiang and G. D. Qian, *Accounts Chem. Res.*, 2010, **43**, 1115-1124.
32. K. K. Tanabe and S. M. Cohen, *Chem. Soc. Rev.*, 2011, **40**, 498-519.
33. S. M. Cohen, *Chem. Rev.*, 2012, **112**, 970-1000.
34. F. X. Llabrés i Xamena, I. Luz and F. G. Cirujano, in *Metal Organic Frameworks as Heterogeneous Catalysts*, eds. F. Llabrés i Xamena and J. Gascon, The Royal Society of Chemistry, 2013, pp. 237-267.
35. J. E. Mondloch, O. K. Farha and J. T. Hupp, in *Metal organic frameworks as heterogeneous catalysts*, eds. F. Llabrés i Xamena and J. Gascon, The Royal Society of Chemistry, Cambridge, 2013, pp. 289-309.
36. A. D. Burrows, in *Metal Organic Frameworks as Heterogeneous Catalysts*, eds. F. Llabrés i Xamena and J. Gascon, The Royal Society of Chemistry, Cambridge, 2013, pp. 31-75.
37. P. Deria, J. E. Mondloch, O. Karagiari, W. Bury, J. T. Hupp and O. K. Farha, *Chem. Soc. Rev.*, 2014, **43**, 5896-5912.
38. J. D. Evans, C. J. Sumby and C. J. Doonan, *Chem. Soc. Rev.*, 2014, **43**, 5933-5951.
39. W. G. Lu, Z. W. Wei, Z. Y. Gu, T. F. Liu, J. Park, J. Park, J. Tian, M. W. Zhang, Q. Zhang, T. Gentle, M. Bosch and H. C. Zhou, *Chem. Soc. Rev.*, 2014, **43**, 5561-5593.
40. B. Y. Li, D. X. Ma, Y. Li, Y. M. Zhang, G. H. Li, Z. Shi, S. H. Feng, M. J. Zaworotko and S. Q. Ma, *Chem. Mater.*, 2016, **28**, 4781-4786.
41. A. Zimpel, T. Preiss, R. Roder, H. Engelke, M. Ingrisch, M. Peller, J. O. Radler, E. Wagner, T. Bein, U. Lachelt and S. Wuttke, *Chem. Mater.*, 2016, **28**, 3318-3326.
42. J. H. Cavka, S. Jakobsen, U. Olsbye, N. Guillou, C. Lamberti, S. Bordiga and K. P. Lillerud, *J. Am. Chem. Soc.*, 2008, **130**, 13850-13851.
43. L. Valenzano, B. Civalieri, S. Chavan, S. Bordiga, M. H. Nilsen, S. Jakobsen, K. P. Lillerud and C. Lamberti, *Chem. Mater.*, 2011, **23**, 1700-1718.
44. S. Chavan, J. G. Vitillo, D. Gianolio, O. Zavorotynska, B. Civalieri, S. Jakobsen, M. H. Nilsen, L. Valenzano, C. Lamberti, K. P. Lillerud and S. Bordiga, *Phys. Chem. Chem. Phys.*, 2012, **14**, 1614-1626.
45. G. C. Shearer, S. Forselv, S. Chavan, S. Bordiga, K. Mathisen, M. Bjorgen, S. Svelle and K. P. Lillerud, *Top. Catal.*, 2013, **56**, 770-782.
46. G. C. Shearer, S. Chavan, J. Ethiraj, J. G. Vitillo, S. Svelle, U. Olsbye, C. Lamberti, S. Bordiga and K. P. Lillerud, *Chem. Mater.*, 2014, **26**, 4068-4071.
47. S. Øien, D. Wragg, H. Reinsch, S. Svelle, S. Bordiga, C. Lamberti and K. P. Lillerud, *Cryst. Growth Des.*, 2014, **14**, 5370-5372.
48. C. A. Trickett, K. J. Gagnon, S. Lee, F. Gandara, H. B. Burgi and O. M. Yaghi, *Angew. Chem.-Int. Edit.*, 2015, **54**, 11162-11167.
49. G. C. Shearer, S. Chavan, S. Bordiga, S. Svelle, U. Olsbye and K. P. Lillerud, *Chem. Mat.*, 2016, **28**, 3749-3761.
50. G. C. Shearer, J. G. Vitillo, S. Bordiga, S. Svelle, U. Olsbye and K. P. Lillerud, *Chem. Mat.*, 2016, **28**, 7190-7193.

51. Y. Bai, Y. B. Dou, L. H. Xie, W. Rutledge, J. R. Li and H. C. Zhou, *Chem. Soc. Rev.*, 2016, **45**, 2327-2367.
52. M. G. Goesten, M. F. de Lange, A. I. Olivos-Suarez, A. V. Bavykina, P. Serra-Crespo, C. Krywka, F. M. Bickelhaupt, F. Kapteijn and J. Gascon, *Nat. Commun.*, 2016, **7**, Art. n. 11832.
53. F. Vermoortele, B. Bueken, G. Le Bars, B. Van de Voorde, M. Vandichel, K. Houthoofd, A. Vimont, M. Daturi, M. Waroquier, V. Van Speybroeck, C. Kirschhock and D. E. De Vos, *J. Am. Chem. Soc.*, 2013, **135**, 11465-11468.
54. M. Lammert, M. T. Wharmby, S. Smolders, B. Bueken, A. Lieb, K. A. Lomachenko, D. De Vos and N. Stock, *Chem. Commun.*, 2015, **51**, 12578-12581.
55. J. Hajek, M. Vandichel, B. Van de Voorde, B. Bueken, D. De Vos, M. Waroquier and V. Van Speybroeck, *J. Catal.*, 2015, **331**, 1-12.
56. D. Yang, S. O. Odoh, T. C. Wang, O. K. Farha, J. T. Hupp, C. J. Cramer, L. Gagliardi and B. C. Gates, *J. Am. Chem. Soc.*, 2015, **137**, 7391-7396.
57. I. Luz, C. Rosler, K. Epp, F. Xamena and R. A. Fischer, *Eur. J. Inorg. Chem.*, 2015, 3904-3912.
58. V. L. Rechac, F. G. Cirujano, A. Corma and F. Xamena, *Eur. J. Inorg. Chem.*, 2016, 4512-4516.
59. R. Dalapati, B. Sakthivel, A. Dhakshinamoorthy, A. Buragohain, A. Bhunia, C. Janiak and S. Biswas, *Crystengcomm*, 2016, **18**, 7855-7864.
60. P. Hester, S. J. Xu, W. Liang, N. Al-Janabi, R. Vakili, P. Hill, C. A. Muryn, X. B. Chen, P. A. Martin and X. L. Fan, *J. Catal.*, 2016, **340**, 85-94.
61. L. G. Ding, B. J. Yao, W. L. Jiang, J. T. Li, Q. J. Fu, Y. A. Li, Z. H. Liu, J. P. Ma and Y. B. Dong, *Inorg. Chem.*, 2017, **56**, 2337-2344.
62. S. Øien-Ødegaard, B. Bouchevreau, K. Hylland, L. P. Wu, R. Blom, C. Grande, U. Olsbye, M. Tilset and K. P. Lillerud, *Inorg. Chem.*, 2016, **55**, 1986-1991.
63. M. Rimoldi, A. J. Howarth, M. R. DeStefano, L. Lin, S. Goswami, P. Li, J. T. Hupp and O. K. Farha, *ACS Catal.*, 2017, **7**, 997-1014.
64. H. Wu, Y. S. Chua, V. Krungleviciute, M. Tyagi, P. Chen, T. Yildirim and W. Zhou, *J. Am. Chem. Soc.*, 2013, **135**, 10525-10532.
65. L. Xu, Y. P. Luo, L. Sun, S. Pu, M. Fang, R. X. Yuan and H. B. Du, *Dalton Trans.*, 2016, **45**, 8614-8621.
66. D. D. Borges, S. Devautour-Vinot, H. Jobic, J. Ollivier, F. Nouar, R. Semino, T. Devic, C. Serre, F. Paesani and G. Maurin, *Angew. Chem.-Int. Edit.*, 2016, **55**, 3919-3924.
67. D. D. Borges, R. Semino, S. Devautour-Vinot, H. Jobic, F. Paesani and G. Maurin, *Chem. Mat.*, 2017, **29**, 1569-1576.
68. G. W. Peterson, J. J. Mahle, J. B. DeCoste, W. O. Gordon and J. A. Rossin, *Angew. Chem.-Int. Edit.*, 2016, **55**, 6235-6238.
69. C. H. Wang, X. L. Liu, J. P. Chen and K. Li, *Sci Rep*, 2015, **5**, 10.
70. Z. G. Hu, A. Nalaparaju, Y. W. Peng, J. W. Jiang and D. Zhao, *Inorg. Chem.*, 2016, **55**, 1134-1141.
71. A. Kronast, S. Eckstein, P. T. Altenbuchner, K. Hindelang, S. I. Vagin and B. Rieger, *Chem.-Eur. J.*, 2016, **22**, 12800-12807.
72. S. Castarlenas, C. Tellez and J. Coronas, *J. Membr. Sci.*, 2017, **526**, 205-211.
73. I. Stassen, B. Bueken, H. Reinsch, J. F. M. Oudenhoven, D. Wouters, J. Hajek, V. Van Speybroeck, N. Stock, P. M. Vereecken, R. Van Schaik, D. De Vos and R. Ameloot, *Chem. Sci.*, 2016, **7**, 5827-5832.
74. S. Jakobsen, D. Gianolio, D. S. Wragg, M. H. Nilsen, H. Emerich, S. Bordiga, C. Lamberti, U. Olsbye, M. Tilset and K. P. Lillerud, *Phys. Rev. B*, 2012, **86**, Art. n. 125429.
75. A. E. Platero-Prats, A. Mavrandonakis, L. C. Gallington, Y. Y. Liu, J. T. Hupp, O. K. Farha, C. J. Cramer and K. W. Chapmant, *J. Am. Chem. Soc.*, 2016, **138**, 4178-4185.
76. M. Lammert, C. Glissmann and N. Stock, *Dalton Trans.*, 2017, **46**, 2425-2429.
77. D. Yang, V. Bernalles, T. Islamoglu, O. K. Farha, J. T. Hupp, C. J. Cramer, L. Gagliardi and B. C. Gates, *J. Am. Chem. Soc.*, 2016, **138**, 15189-15196.
78. C. Atzori, G. C. Shearer, L. Maschio, B. Civalieri, F. Bonino, C. Lamberti, S. Svelle, K. P. Lillerud and S. Bordiga, *J. Phys. Chem. C*, 2017, **121**, 9312-9324.
79. M. Lammert, C. Glissmann, H. Reinsch and N. Stock, *Cryst. Growth Des.*, 2017, **17**, 1125-1131.
80. V. V. Butova, A. P. Budnyk, A. A. Guda, K. A. Lomachenko, A. L. Bugaev, A. V. Soldatov, S. M. Chavan, S. Øien-Ødegaard, U. Olsbye, K. P. Lillerud, C. Atzori, S. Bordiga and C. Lamberti, *Cryst. Growth Design*, 2017, **17**, doi: 10.1021/acs.cgd.1027b00892.
81. M. Kandiah, M. H. Nilsen, S. Usseglio, S. Jakobsen, U. Olsbye, M. Tilset, C. Larabi, E. A. Quadrelli, F. Bonino and K. P. Lillerud, *Chem. Mat.*, 2010, **22**, 6632-6640.
82. S. J. Garibay and S. M. Cohen, *Chem. Commun.*, 2010, **46**, 7700-7702.
83. M. J. Katz, Z. J. Brown, Y. J. Colon, P. W. Siu, K. A. Scheidt, R. Q. Snurr, J. T. Hupp and O. K. Farha, *Chem. Commun.*, 2013, **49**, 9449-9451.
84. C. Kutzscher, G. Nickerl, I. Senkovska, V. Bon and S. Kaskel, *Chem. Mater.*, 2016, **28**, 2573-2580.

85. K. T. Hylland, S. Oien-Odegaard, K. P. Lillerud and M. Tilset, *Synlett*, 2015, **26**, 1480-1485.
86. N. C. Thacker, P. Ji, Z. Lin, A. Urban and W. Lin, *Faraday Discuss.*, 2017, **201**, 303-315.
87. M. I. Gonzalez, J. Oktawiec and J. R. Long, *Faraday Discuss.*, 2017, **201**, 351-367.
88. Y. Y. Liu, K. Leus, T. Bogaerts, K. Hemelsoet, E. Bruneel, V. Van Speybroeck and P. Van Der Voort, *ChemCatChem*, 2013, **5**, 3657-3664.
89. P. Valvekens, E. D. Bloch, J. R. Long, R. Ameloot and D. E. De Vos, *Catal. Today*, 2015, **246**, 55-59.
90. T. Toyao, K. Miyahara, M. Fujiwaki, T. H. Kim, S. Dohshi, Y. Horiuchi and M. Matsuoka, *J. Phys. Chem. C*, 2015, **119**, 8131-8137.
91. L. Braglia, E. Borfecchia, L. Maddalena, S. Øien, K. A. Lomachenko, A. L. Bugaev, S. Bordiga, A. V. Soldatov, K. P. Lillerud and C. Lamberti, *Catal. Today*, 2017, **283**, 89-103.
92. L. Braglia, E. Borfecchia, K. A. Lomachenko, A. L. Bugaev, A. A. Guda, A. V. Soldatov, B. T. L. Bleken, S. Oien, U. Olsbye, K. P. Lillerud, S. Bordiga, G. Agostini, M. Manzoli and C. Lamberti, *Faraday Discuss.*, 2017, doi: 10.1039/C1037FD00024C.
93. C. Wang, Z. G. Xie, K. E. deKrafft and W. L. Lin, *J. Am. Chem. Soc.*, 2011, **133**, 13445-13454.
94. C. H. Hendon, J. Bonnefoy, E. A. Quadrelli, J. Canivet, M. B. Chambers, G. Rousse, A. Walsh, M. Fontecave and C. Mellot-Draznieks, *Chem.-Eur. J.*, 2016, **22**, 3713-3718.
95. L. Braglia, E. Borfecchia, K. Lomachenko, S. Øien, K. Lillerud and C. Lamberti, *Journal of Physics: Conference Series*, 2016.
96. H. H. Fei and S. M. Cohen, *Chem. Commun.*, 2014, **50**, 4810-4812.
97. T. H. Zhou, Y. H. Du, A. Borgna, J. D. Hong, Y. B. Wang, J. Y. Han, W. Zhang and R. Xu, *Energy Environ. Sci.*, 2013, **6**, 3229-3234.
98. S. Øien, G. Agostini, S. Svelle, E. Borfecchia, K. A. Lomachenko, L. Mino, E. Gallo, S. Bordiga, U. Olsbye, K. P. Lillerud and C. Lamberti, *Chem. Mater.*, 2015, **27**, 1042-1056.
99. E. Borfecchia, S. Øien, S. Svelle, L. Mino, L. Braglia, G. Agostini, E. Gallo, K. Lomachenko, S. Bordiga, A. Guda, S. M. A., A. V. Soldatov, U. Olsbye, K. P. Lillerud and C. Lamberti, 2016, **712**, 012125.
100. E. Reddington, A. Sapienza, B. Gurau, R. Viswanathan, S. Sarangapani, E. S. Smotkin and T. E. Mallouk, *Science*, 1998, **280**, 1735-1737.
101. J. Pérez-Ramírez, F. Kapteijn, K. Schöffel and J. A. Moulijn, 2003, **44**, 117-151.
102. R. Kopelent, J. A. van Bokhoven, J. Szlachetko, J. Edebeli, C. Paun, M. Nachttegaal and O. V. Safonova, *Angew. Chem. Int. Ed.*, 2015, **54**, 8728-8731.
103. A. T. Bell, *Science*, 2003, **299**, 1688-1691.
104. A. T. Nielsen, 1962, **27**, 1998-2001.
105. G. F. Santori, A. G. Moglioni, V. Vetere, G. Y. M. Iglesias, M. L. Casella and O. A. Ferretti, *Appl. Catal. A: General*, 2004, **269**, 215-223.
106. X.-F. Yang, A. Wang, B. Qiao, J. Li, J. Liu and T. Zhang, *Acc. Chem. Res.*, 2013, **46**, 1740-1748.
107. M. Meilikhov, K. Yusenko, D. Esken, S. Turner, G. Van Tendeloo and R. A. Fischer, *Eur. J. Inorg. Chem.*, 2010, **2010**, 3701-3714.
108. I. Luz, A. Louidice, D. T. Sun, W. L. Queen and R. Buonsanti, *Chem. Mater.*, 2016, **28**, 3839-3849.
109. K. Na, K. Choi, O. M. Yaghi and G. A. Somorjai, *Nano Lett.*, 2014, **14**, 5979-5983.
110. A. E. Shilov and G. B. Shul'pin, *Chem. Rev.*, 1997, **97**, 2879-2932.
111. R. A. Periana, D. J. Taube, S. Gamble, H. Taube, T. Satoh and H. Fujii, *Science*, 1998, **280**, 560-564.
112. J. A. Labinger and J. E. Bercaw, *Nature*, 2002, **417**, 507-514.
113. M. Lersch and M. Tilset, *Chem. Rev.*, 2005, **105**, 2471-2526.
114. R. Palkovits, M. Antonietti, P. Kuhn, A. Thomas and F. Schüth, *Angew. Chem.-Int. Edit.*, 2009, **48**, 6909-6912.
115. R. Palkovits, C. von Malotki, M. Baumgarten, K. Mullen, C. Baltes, M. Antonietti, P. Kuhn, J. Weber, A. Thomas and F. Schüth, *ChemSusChem*, 2010, **3**, 277-282.
116. E. S. Gutterød, S. Øien-Ødegaard, K. Bossers, A.-E. Nieuwelink, M. Manzoli, L. Braglia, A. Lazzarini, E. Borfecchia, S. Ahmadigoltapeh, B. Bouchevrau, B. T. Lønstad-Bleken, R. Henry, C. Lamberti, S. Bordiga, B. M. Weckhuysen, K. P. Lillerud and U. Olsbye, *Ind. Eng. Chem. Res.*, 2017, **56**, doi: 10.1021/acs.iecr.1027b01457.
117. S. Brunauer, P. H. Emmett and E. Teller, *J. Am. Chem. Soc.*, 1938, **60**, 309-319.
118. K. S. W. Sing, in *Adsorption by Powders and Porous Solids (Second Edition)*, eds. F. Rouquerol, J. Rouquerol, K. S. W. Sing, P. Llewellyn and G. Maurin, Academic Press, Oxford, 2014, pp. 237-268.
119. W. van Beek, O. V. Safonova, G. Wiker and H. Emerich, *Phase Transit.*, 2011, **84**, 726-732.
120. P. M. Abdala, O. V. Safonova, G. Wiker, W. van Beek, H. Emerich, J. A. van Bokhoven, J. Sa, J. Szlachetko and M. Nachttegaal, *Chimia*, 2012, **66**, 699-705.
121. A. L. Bugaev, A. A. Guda, K. A. Lomachenko, V. V. Shapovalov, A. Lazzarini, J. G. Vitillo, L. A. Bugaev, E. Groppo, R. Pellegrini, A. V. Soldatov, J. A. van Bokhoven and C. Lamberti, *J. Phys. Chem. C*, 2017, **121**, 18202-18213.

122. S. Bordiga, E. Groppo, G. Agostini, J. A. van Bokhoven and C. Lamberti, *Chem. Rev.*, 2013, **113**, 1736-1850.
123. C. Lamberti, S. Bordiga, F. Bonino, C. Prestipino, G. Berlier, L. Capello, F. D'Acapito, F. X. L. I. Xamena and A. Zecchina, *Phys. Chem. Chem. Phys.*, 2003, **5**, 4502-4509.
124. J. Kieffer and J. P. Wright, *Powder Diffract.*, 2013, **28**, S339-S350.
125. V. Petříček, M. Dušek and L. Palatinus, *Z. Kristallog.*, 2014, **229**, 345-352.
126. C. Lamberti, C. Prestipino, S. Bordiga, G. Berlier, G. Spoto, A. Zecchina, A. Laloni, F. La Manna, F. D'Anca, R. Felici, F. D'Acapito and P. Roy, *Nucl. Instrum. Methods Phys. Res. Sect. B-Beam Interact. Mater. Atoms*, 2003, **200**, 196-201.
127. T. M. Grehk and P. O. Nilsson, *Nucl. Instrum. Methods Phys. Res. Sect. A-Accel. Spectrom. Dect. Assoc. Equip.*, 2001, **467**, 635-638.
128. S. Carlson, M. Clausen, L. Gridneva, B. Sommarin and C. Svensson, *J. Synchrot. Radiat.*, 2006, **13**, 359-364.
129. M. Nachtegaal, O. Müller, C. König and R. Frahm, in *X-Ray Absorption and X-Ray Emission Spectroscopy: Theory and Applications*, eds. J. A. van Bokhoven and C. Lamberti, John Wiley & Sons, Chichester (UK), 2016, vol. I, pp. 155-183.
130. B. Ravel and M. Newville, *J. Synchrotron Radiat.*, 2005, **12**, 537-541.
131. C. Lamberti, S. Bordiga, D. Arduino, A. Zecchina, F. Geobaldo, G. Spanò, F. Genoni, G. Petrini, A. Carati, F. Villain and G. J. Vlaic, *J. Phys. Chem. B*, 1998, **102**, 6382-6390.
132. S. I. Zabinsky, J. J. Rehr, A. Ankudinov, R. C. Albers and M. J. Eller, *Phys. Rev. B*, 1995, **52**, 2995-3009.
133. M. Newville, *J. Synchrotron Radiat.*, 2001, **8**, 322-324.
134. G. Dalba and P. Fornasini, *J. Synchrot. Radiat.*, 1997, **4**, 243-255.
135. A. Einstein, *Ann. Phys.*, 1907, **22**, 180-190.
136. A. P. Menushenkov, S. Benazeth, J. Purans, A. Y. Ignatov and K. V. Klementev, *Physica C*, 1997, **277**, 257-264.
137. N. VanHung and J. J. Rehr, *Phys. Rev. B*, 1997, **56**, 43-46.
138. G. Dalba, P. Fornasini, R. Grisenti and J. Purans, *Phys. Rev. Lett.*, 1999, **82**, 4240-4243.
139. P. Ghigna, A. Carollo, G. Flor, L. Malavasi and G. S. Peruga, *J. Phys. Chem. B*, 2005, **109**, 4365-4372.
140. L. L. Araujo, P. Kluth, G. D. M. Azevedo and M. C. Ridgway, *Phys. Rev. B*, 2006, **74**, Art. n. 184102.
141. C. S. Schnohr, P. Kluth, L. L. Araujo, D. J. Sprouster, A. P. Byrne, G. J. Foran and M. C. Ridgway, *Phys. Rev. B*, 2009, **79**, Art. n. 195203.
142. D. J. Sprouster, R. Giulian, L. L. Araujo, P. Kluth, B. Johannessen, D. J. Cookson, G. J. Foran and M. C. Ridgway, *J. Appl. Phys.*, 2010, **107**, Art. n. 014313.
143. G. Bunker, *Introduction to XAFS A Practical Guide to X-ray Absorption Fine Structure Spectroscopy*, Cambridge University Press, Cambridge, 2010.
144. A. Agostini, R. Grisenti, C. Lamberti, A. Piovano and P. Fornasini, *J. Phys.: Conf. Ser.*, 2013, **430**, Art. n. 012031.
145. T. Yokoyama, K. Asakura, Y. Iwasawa and H. Kuroda, *J. Phys. Chem.*, 1989, **93**, 8323-8327.
146. H. Kuroda, T. Yokoyama, K. Asakura and Y. Iwasawa, *Faraday Discuss.*, 1991, **92**, 189-198.
147. N. Van Hung and J. J. Rehr, *Phys. Rev. B*, 1997, **56**, 43-46.
148. G. W. Stinton and J. S. O. Evans, *J. Appl. Crystallogr.*, 2007, **40**, 87-95.
149. G. Agostini, C. Lamberti, L. Palin, M. Milanesio, N. Danilina, B. Xu, M. Janousch and J. A. van Bokhoven, *J. Am. Chem. Soc.*, 2010, **132**, 667-678.
150. E. Groppo, C. Prestipino, C. Lamberti, P. Luches, C. Giovanardi and F. Boscherini, *J. Phys. Chem. B*, 2003, **107**, 4597-4606.
151. C. Lamberti, E. Groppo, C. Prestipino, S. Casassa, A. M. Ferrari, C. Pisani, C. Giovanardi, P. Luches, S. Valeri and F. Boscherini, *Phys. Rev. Lett.*, 2003, **91**, 046101.
152. L. Salassa, E. Borfecchia, T. Ruiu, C. Garino, D. Gianolio, R. Gobetto, P. J. Sadler, M. Cammarata, M. Wulff and C. Lamberti, *Inorg. Chem.*, 2010, **49**, 11240-11248.
153. G. Agostini, S. Usseglio, E. Groppo, M. J. Uddin, C. Prestipino, S. Bordiga, A. Zecchina, P. L. Solari and C. Lamberti, *Chem. Mat.*, 2009, **21**, 1343-1353.
154. S. Pascarelli, F. Boscherini, C. Lamberti and S. Mobilio, *Phys. Rev. B*, 1997, **56**, 1936-1947.
155. G. Agostini, A. Piovano, L. Bertinetti, R. Pellegrini, G. Leofanti, E. Groppo and C. Lamberti, *J. Phys. Chem. C*, 2014, **118**, 4085-4094.
156. A. I. Frenkel, C. W. Hills and R. G. Nuzzo, *J. Phys. Chem. B*, 2001, **105**, 12689-12703.
157. G. Agostini, R. Pellegrini, G. Leofanti, L. Bertinetti, S. Bertarione, E. Groppo, A. Zecchina and C. Lamberti, *J. Phys. Chem. C*, 2009, **113**, 10485-10492.
158. J. E. Huheey, E. A. Keiter and R. L. Keiter, *Inorganic Chemistry: Principles of Structure and Reactivity (4th Ed.)*, 4th edn., Harpercollins College, New-York, 1993.

159. S. Calvin, M. M. Miller, R. Goswami, S.-F. Cheng, S. P. Mulvaney, L. J. Whitman and V. G. Harris, 2003, **94**, 778-783.
160. A. I. Frenkel, A. Yeveck, C. Cooper and R. Vasic, in *Annual Review of Analytical Chemistry, Vol 4*, eds. R. G. Cooks and E. S. Yeung, Annual Reviews, Palo Alto, 2011, vol. 4, pp. 23-39.
161. C. Solliard and M. Flueli, *Surf. Sci.*, 1985, **156**, 487-494.
162. A. Pinto, A. R. Pennisi, G. Faraci, G. Dagostino, S. Mobilio and F. Boscherini, *Phys. Rev. B*, 1995, **51**, 5315-5321.
163. W. H. Qi and M. P. Wang, *J Nanopart Res*, 2005, **7**, 51-57.
164. G. Smolentsev and A. V. Soldatov, *Comput. Mater. Sci.*, 2007, **39**, 569-574.
165. E. R. Malinowski, *Factor Analysis in Chemistry*, 3rd Ed., Wiley, Chichester, 2002.
166. E. R. Malinowski, *Anal. Chem.*, 1977, **49**, 612-617.
167. A. Martini, E. Borfecchia, K. A. Lomachenko, I. A. Pankin, C. Negri, G. Berlier, P. Beato, H. Falsig, S. Bordiga and C. Lamberti, *Chem. Sci.*, 2017, **8**, doi: 10.1039/C1037SC02266B.
168. E. R. Malinowski, *Factor Analysis in Chemistry*, Wiley, 1991.
169. A. Elbergali, J. Nygren and M. Kubista, *Anal. Chim. Acta*, 1999, **379**, 143-158.
170. B. K. Dable and K. S. Booksh, *J. Chemometr.*, 2001, **15**, 591-613.
171. A. Manceau, M. Marcus and T. Lenoir, *J. Synchrot. Radiat.*, 2014, **21**, 1140-1147.
172. K. A. Lomachenko, E. Borfecchia, C. Negri, G. Berlier, C. Lamberti, P. Beato, H. Falsig and S. Bordiga, *J. Am. Chem. Soc.*, 2016, **138**, 12025-12028.
173. Y. Tulchinsky, C. H. Hendon, K. A. Lomachenko, E. Borfecchia, B. C. Melot, M. R. Hudson, J. D. Tarver, M. D. Korzynski, A. W. Stubbs, J. J. Kagan, C. Lamberti, C. M. Brown and M. Dinca, *J. Am. Chem. Soc.*, 2017, **139**, 5992-5997.
174. C. W. Andersen, E. Borfecchia, M. Bremholm, M. R. V. Jørgensen, P. N. R. Vennestrøm, C. Lamberti, L. F. Lundegaard and B. B. Iversen, *Angew. Chem. Int.-Ed.*, 2017, **56**, 10367-10372.